OPTICAL FORCE REGULATION WITH NANOSTRUCTURED MATERIALS

A Dissertation

Submitted to the Faculty

of

Purdue University

by

Li-Fan Yang

In Partial Fulfillment of the

Requirements for the Degree

of

Doctor of Philosophy

May 2020

Purdue University

West Lafayette, Indiana

THE PURDUE UNIVERSITY GRADUATE SCHOOL
STATEMENT OF DISSERTATION APPROVAL

Dr. Kevin Webb, Chair

School of Electrical and Computer Engineering

Dr. Xianfan Xu

School of Electrical and Computer Engineering

Dr. Daniel Elliott

School of Electrical and Computer Engineering

Dr. Peter Bermel

School of Electrical and Computer Engineering

Approved by:

Dr. Dimitrios Peroulis

Head of the School Graduate Program

To my family, whose support, patience, and love made this possible.

ACKNOWLEDGMENTS

This work would not have been possible without the guidance and support of my professors, peers, family, and friends. In particular, I would like to express my sincere gratitude to my advisor Kevin Webb for his optimistic outlook and assiduous drive for true knowledge and important understanding. I would also like to thank Xianfan Xu, Daniel Elliott, and Peter Bermel for being on my committee, and especially to Xianfan Xu for his great support to the experiment. I thank Anurup Datta and Yu-Chun for their contributions to the projects we worked on together. I also thank the rest of our group members, Brian, Dergan, Ryan, Vivek, and Adam, just to name a few, for their support and friendship over the years.

TABLE OF CONTENTS

Page

LIST OF FIGURES

Figure Page

Figure Page

Figure Page

Figure Page

Figure Page

Figure Page

Figure Page

ABSTRACT

Li-Fan Yang Ph.D., Purdue University, May 2020. Optical Force Regulation with Nanostructured Materials. Major Professor: Kevin J. Webb.

The use of light to control mechanical systems is of broad importance in science and technology. From Maxwell's theory, the maximum optical pressure on a mirror is twice the average incident power density divided by the velocity of light. Here it is experimentally demonstrated that, with a specially designed nanostructured membrane, the optical pressure substantially exceeds that on a perfect mirror. Enhanced pressure is demonstrated by deflection measurement of a patterned gold film on a silicon nitride membrane, in conjunction with a model and with established error bounds to draw definitive conclusions. The enhancement of the net optical pressure with nanostructured material over that on a perfect mirror can be understood as being due to an asymmetric cavity effect within a modest quality factor regime, and this is illustrated using a simple one-dimensional model. Therefore, carefully harnessing the photon confinement in nanostructured material leads to pressure enhancement.

The physical basis of a net pulling force on a structure is presented. Whether there is a pushing or a pulling pressure can be regulated by excitation of a surface wave on the front or back side of a nanostructured metal film. This can be achieved through geometrical and material design, and it is shown that pushing or pulling with a single structure, depending on wavelength, is possible. Furthermore, an enhanced pulling pressure can also be achieved in a simple all-dielectric silicon-based system. Various applications will benefit from optomechanics with pushing or pulling achieved by control of the characteristic of the incident light.

1. INTRODUCTION

It has been more than a century now since the radiation pressure experimental work by Nichols and Hull and also Lebedev confirmed that light can impart a mechanical force on matter [1, 2], in a manner consistent with the prediction of J. C. Maxwell [3]. Radiation pressure is now used to propel spacecrafts. Furthermore, the laser tweezing work of Ashkin [4, 5] and others has led to instruments that are important for molecular biology [6,7], where beads with the biomolecules attached are moved by a laser. Concomitant understanding of laser trapping has been important in trapping atoms and realizing condensates, as is critical in precise clocks that have broad impact [8–10]. All of this work has relied on planar or homogeneous materials, such as is used in forming mirrors or beads. While a bead can be moved back and forth in a trap, radiation pressure pushes a planar mirror. Therefore, some other force is needed to return the structure to the original position or move it in another way. While strain can do so, the control is poor. Being able to push or pull a structure is important in many applications that could be served by optical force actuation, such as beam or signal control for low-energy, all-optical communication.

A body of theoretical work, for example [11, 12], suggests that the Einstein-Laub force density expression [13] can explain key optical force experimental results. Two important experiments in this regard are the 1978 Jones and Leslie mirror experiment [14] and the 1973 Ashkin and Dziedzic water experiment [4]. Lacking is specific force density data that can be used to establish a predictive model for design. This can be interpreted as a need for a combined nanometer-scale force experiment and model development or a confirmation effort. A lack of such a rigorous combined theoretical and experimental description has hampered optomechanics and the exploitation of the mechanical aspects of light and, more generally, electromagnetics.

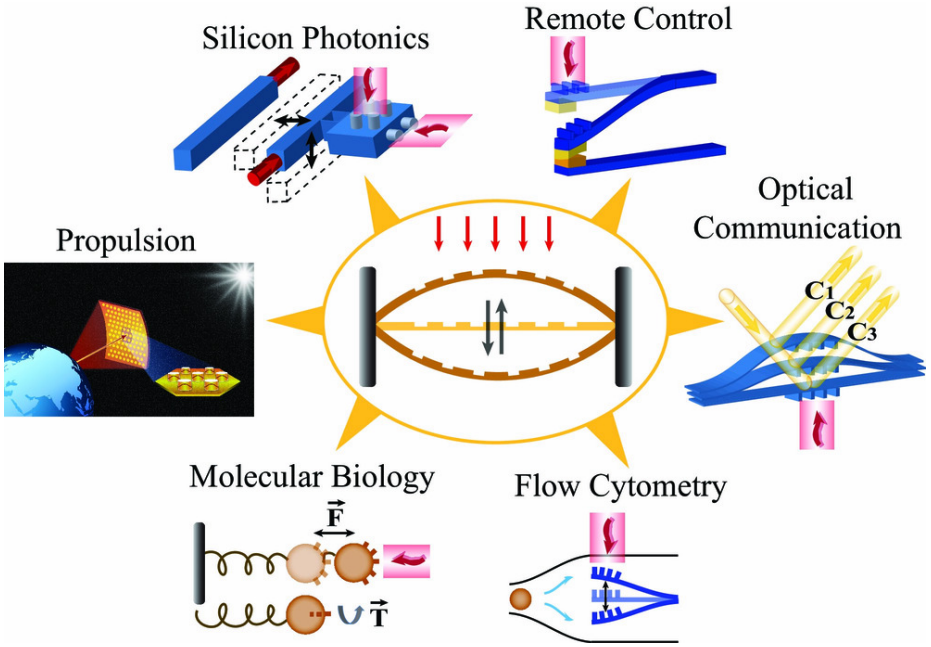

Fig. 1.1. Example application space for a nanostructured surface. The central figure presents the pushing and pulling concept from an incident plane wave (red arrows) in the way of direction control (black arrows). The satellite figures shows the potential applications of optical communication, silicon photonics, and propulsion.

By applying the Einstein-Laub force density, we investigate and show that nanostructured materials will allow overall pushing and pulling pressure from light and develop a designing methodology. The concept and a suite of applications is illustrated in Fig. 1.1. The center figure shows nanostructured material with a wave incident from single direction and a pushing force (in the direction of incident light) and pulling force (in the opposite direction). The satellite images portray a variety of applications.

In this thesis, we present a combined numerical simulation and design method based on field solutions incorporated into a force density description. This is used to develop an understanding of the relationship between structured material and force. Experimental work to determine the deflection of a patterned membrane due to a laser confirms that a pressure greater than that on a planar perfect mirror is possible.

With simulations, understanding of how to regulate surface waves on the front and back of a structure leads to understanding of how to regulate the optical force and to achieve either a pushing or a pulling force.

Chapter 2 summarizes the electromagnetic force model we utilized. In Chapter 3, we present our primary work on the experimental demonstration that optical pressure on a nanostructured surface can be enhanced, greater than that on a perfect mirror, with the use of structured material and exploiting the third dimension [15]. This can be understood as an asymmetric cavity effect, as described in Chapter 4, with control of quality factor (Q) and mirror reflection coefficients, and there is a straight forward explanation with a 1D cavity [16]. In Chapter 5, we discuss the enhanced pushing and pulling force achieved by exciting plasmon surface waves on a nanoslotted metal membrane incorporating a silicon nitride (SiN) layer. By regulating the geometry and the metal-insulator-metal (MIM) cavity mode, excitation of a surface wave on the front side (incident wave side) or the back side (the opposite side) of the membrane allows a collective pushing or pulling pressure, respectively. These results involve metal and dielectric materials. Applications of metals in optomechanics provides for surface waves and very small resonant cavities, and both pushing and pulling. However, metals are relatively lossy and will heat. Consequently undesirable thermal-based deflection may occur. Also, in certain applications it may be preferable to use an all-dielectric material system. In Chapter 6 we investigate the enhanced optical pressure in an all-dielectric material system with the band gap beyond the incident wavelength to avoid thermal issues. In this initial work, we propose two approaches that allow a pulling force in the dielectric material. The first approach induces the pulling force in a low refractive index layer sandwiched between two high refractive index layers, following earlier work showing analytic solutions for the force on a slab in some background material [17]. The second approach utilizes evanescent fields from total internal reflection. The field solution from the evanescent field nature provides the condition for the gradient force to become significant and to provide a pulling force in the material.

2. OPTICAL FORCE MODELING AND OPTICAL FORCE ON STRUCTURED MATERIAL

2.1 Optical Force Modeling

The pressure on a mirror can be understood at the atomic level, where there is a momentum exchange between the photon and the atom that can be influenced by the environment [18]. From Maxwell's picture, at the macroscopic material level, the optical force on a surface has been described by a pressure [3]

$$P = \frac{S(1 + |\Gamma|^2)}{v}, \tag{2.1}$$

where S is the time-averaged normally-incident Poynting vector magnitude ($\mathrm{W/m^2}$), Γ is the field reflection coefficient, and v is the wave velocity in the background, assumed to be c, the speed of light in vacuum, in this work. Consequently, the maximum pressure, which is on a perfect mirror, from (2.1) is $P = 2S/c$ $\mathrm{N/m^2}$. However, (2.1) precludes information on how the field interacts with the material.

A fundamental approach is to describe the optical force density in the material in terms of fields. We utilize the Einstein and Laub force density in material [13], as we have in our previous work [17, 19–21], and as used by others [12, 22]. Using this description, the electromagnetic kinetic force density in material media becomes

$$\mathbf{f} = \frac{\partial \mathbf{P}}{\partial t} \times \mu_0 \mathbf{H} - \frac{\partial \mu_0 \mathbf{M}}{\partial t} \times \epsilon_0 \mathbf{E} + \rho \mathbf{E} - \mu_0 \mathbf{H} \times \mathbf{J} + (\mathbf{P} \cdot \nabla)\mathbf{E} + \mu_0 (\mathbf{M} \cdot \nabla)\mathbf{H}, \tag{2.2}$$

with $\mathbf{f}$ having SI units of $\mathrm{N/m^3}$ and $\mathbf{P}$ the polarization, $\mathbf{M}$ the magnetization, $\mathbf{J}$ the free electric current density, ρ the free electric charge density, μ_0 is the permeability of free space, and ϵ_0 the permittivity of free space. We consider a time-harmonic, monochromatic field with frequency dependence $\exp(j\omega t)$ and an isotropic dielectric response, giving $\mathbf{P}(\mathbf{r}, \omega) = \epsilon_0 \chi_E(\mathbf{r}, \omega)\mathbf{E}(\mathbf{r}, \omega)$, with χ_E the complex electric suscepti-

bility (and dielectric constant $\epsilon = 1 + \chi_E$). The time average of the force density in the frequency domain assuming source-free with dielectric media (2.2) becomes

$$\langle \mathbf{f} \rangle = (-\hat{\mathbf{e}} \times \hat{\mathbf{h}}) \frac{\mu_0 \epsilon_0 \omega}{2} \Im\{\chi_E E(\mathbf{r}) H^*(\mathbf{r})\} + \frac{\epsilon_0}{2} \Re\{(\chi_E E(\mathbf{r}))\ \hat{\mathbf{e}} \cdot \nabla)(\hat{\mathbf{e}} E^*(\mathbf{r}))\}, \quad (2.3)$$

where $\Re\{\cdot\}$ is the real part and $\Im\{\cdot\}$ is the imaginary part, E is the phasor electric field and H the phasor magnetic field, and $\hat{\mathbf{e}}$ and $\hat{\mathbf{h}}$ their respective unit vectors. Following a numerical solution for the fields, we use (2.3) to obtain the time-averaged force density, and then form the total force and hence the pressure ($\mathrm{N/m^2}$) by ascribing an area such as the unit cell in a periodic system. Then the time-averaged pressure is then calculated by integrating the force density over the unit cell area and dividing by the unit cell width. Conservation of momentum is inherent in use of (2.3) because this kinetic force density is formed with use of the classical field momentum [11, 13, 23].

2.2 Resonant Fields in an Array of Cavities in Gold

In previous work, the simulated pressure on structured material was presented and the possibility of a pressure greater than on a perfect mirror proposed [24]. We provide some background on this work as motivation for the results described in this thesis. Consider the structured Gold (Au) metal film in Fig. 2.1 with free space above and below. A 2D numerical finite element method solution [25] for the fields used periodic boundary conditions on the left and right and assumed a plane wave normally incident from above with E_x, H_z (note the coordinate system in the lower left of Fig. 2.1). A wavelength of 632.8 nm was used and the complex dielectric constant for Au was taken from the literature [26]. With the polarization considered, plasmonic cavity modes, with the basis of resonant metal-insulator-metal (MIM) slot mode, can form in the slot [27].

A number of structures were analyzed to evaluate the influence of a nanostructured surface on the optical force experienced by the sample. In order to consider a situation representative of an experiment, the Poynting vector of the incident plane wave was normalized for an illumination power density equivalent to 1 mW over a

uniformly illuminated circular spot size of diameter 1 μm. The average force density was calculated from (2.3) using the numerical solutions for the fields for slot widths (W) of 30 nm and 60 nm, and a sequence of depths (D), and upon integration over the thickness of the film, found the pressure on the Au film, $P = \langle p_y \rangle$. Plots of the normal component of the time-average force density, $\langle f_y \rangle$, are given in Fig. 2.2(a)-(c) for a 30 nm wide slot and slot depths of 1, 51, and 81 nm. Notice that the force distribution in the material varies considerably as a function of slot depth. In order to develop a better picture of the relative force as a function of slot geometry, Fig. 2.2(d) gives the pressure for the 30 nm and 60 nm slot widths as a function of slot depth with a (normalized) input power density of 1 W/m^2. The maximum pressure occurs at the resonant depth, and the peak pressure is higher for the 30 nm slot case. The result indicates a pressure that is about one order of magnitude higher than that on a perfect mirror. This enhancement can be understood as being due to an asymmetric cavity [16] and has been verified in experiments [15], that will be discussed in the following sections.

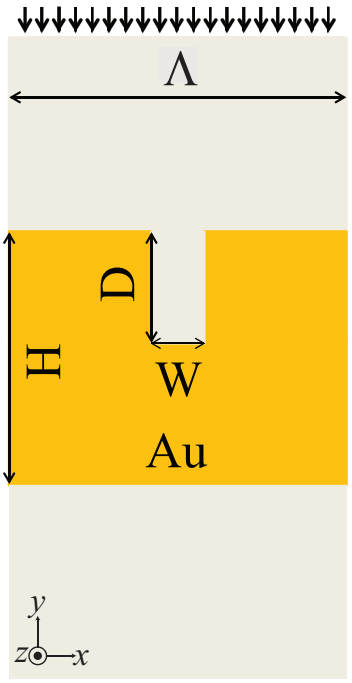

Fig. 2.1. Simulated gold (Au) metal film structures in free space: D is varied between 1 nm and 90 nm, with W set to 30 nm and 60 nm. In all cases, the Au sample is illuminated from the top by 632.8 nm light (E_x, H_z), Λ is 400 nm, H is 200 nm. Periodic boundary conditions are enforced on the left and right, and port boundaries are on the top and bottom. The figure is taken from [24].

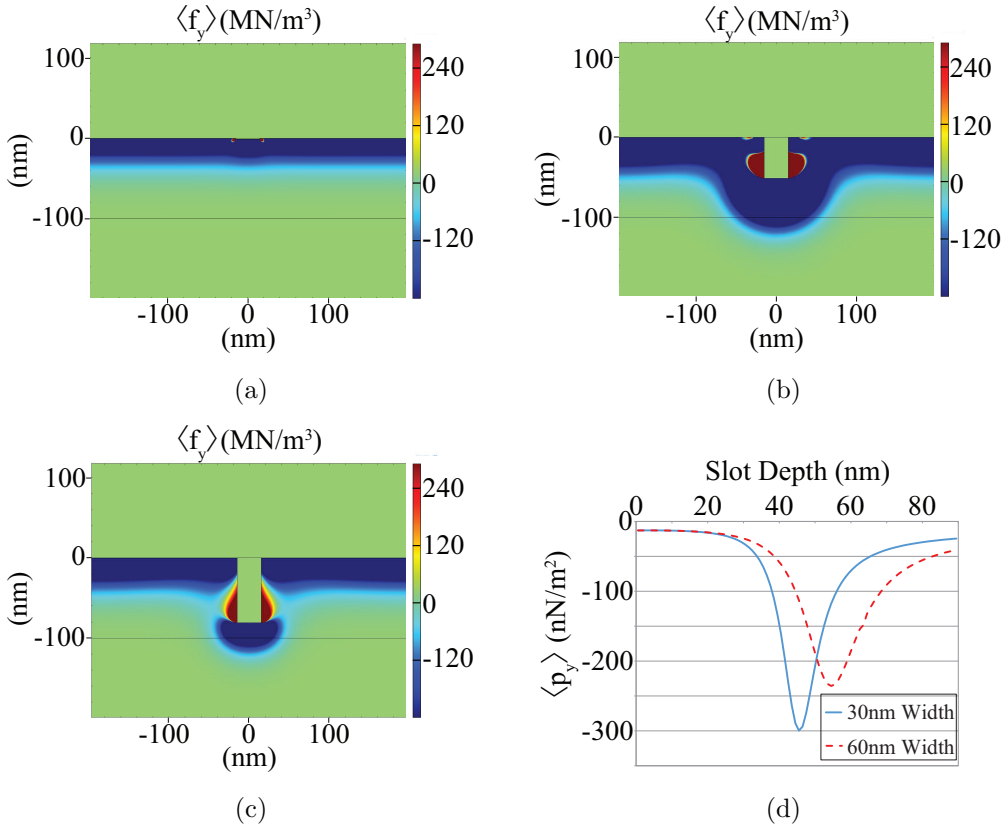

Fig. 2.2. The normal ($y-$component) of the force density for a 30 nm wide slot in Au at various slot depths: (a) 1 nm; (b) 51 nm: (c) 81 nm. The simulation has an incident power density equivalent to 1 mW of 632.8 nm laser illumination over a circular spot of diameter 1 μm. For reference, resonance is achieved at about 46 nm for the 30 nm wide slot. (d) Numerical results for the pressure as a function of slot depth in a Au film for the two slot widths, calculated for slot depths from 1 nm to 90 nm in 1 nm steps and the pressure $P = \langle p_y \rangle$, in N/m^2 determined by integrating the $y-$component of force density over the depth of the Au nanostructure. These values are normalized to a Poynting vector power density of 1 W/m^2 and the wavelength is 632.8 nm. The figure is taken form [24].

3. DEMONSTRATION OF ENHANCED OPTICAL PRESSURE ON A STRUCTURED SURFACE[†]

The interaction of electromagnetic waves with condensed matter and the resultant force is fundamental in the physical sciences. The maximum pressure on a planar surface is understood to be twice the incident wave power density normalized by the background velocity. We demonstrate for the first time that this pressure can be exceeded by a substantial factor by structuring a surface. Experimental results for direct optomechanical deflection of a nanostructured gold film on a silicon nitride membrane illuminated by a laser beam are shown to significantly exceed those for the planar surface. This enhanced pressure can be understood as being associated with an asymmetric optical cavity array realized in the membrane film. The possible enhancement depends on the material properties and the geometrical parameters of the structured material. Such control and increase of optical pressure with nanostructured material should impact applications across the physical sciences.

Li-Fan is responsible for the design and simulation, experiment, and data analysis with great assistant from Anurup Datta on the membrane fabrication and also the experiment.

3.1 Introduction

We demonstrate that the optical force on a material is sensitive to the surface structure and show that the pressure can be substantially larger than on a planar surface. By measuring the deflection of a membrane having a patterned metal surface, shown schematically in Fig. 3.1(a), we present experimental confirmation of the

[†] This work is published as
L. -F. Yang, A. Datta, Y. -C. Hsueh, X. Xu, and K. J. Webb, "Demonstration of enhanced optical pressure on a structured surface," *Phys. Rev. Lett.*, 122(8), 083901, 2019 (Ref. [15])

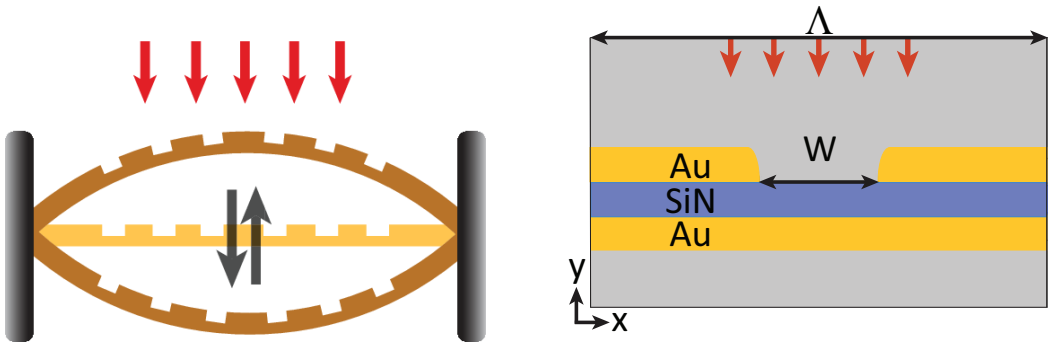

(a) (b)

Fig. 3.1. (a) The structuring of the surface of a metal film with an array of resonant cavities can result in an increase in the optical pushing and pulling force (black arrows), relative to that on a prefect mirror and a planar surface. The red arrows indicate the direction of the incident light. (b) Simulated structure with a periodic boundary (left and right) and parameters: period Λ, slot width W, Au thickness 50 nm, and SiN thickness 50 nm. We consider deflection with a laser having a free space wavelength of 1070 nm.

enhanced pressure on a surface that was previously proposed [24]. The physical basis of the enhancement is an asymmetric resonant cavity array that provides for an increase in the net pressure. In this way, the structured surface is increasing the pressure by providing a further nanometer-scale spatial dimension for the interaction of the light with the material.

The pressure on a planar mirror from Maxwell's picture [3] can be expressed as (2.1). From this picture, the conventional maximum pressure is $P = 2S/c$ N/m^2. A fundamental approach is to describe the optical force density in the material in terms of fields. We utilized the Einstein and Laub force density in material [13], shown as (2.2) with (2.3) the averaged term assuming monochromatic field, source free, and an isotropic dielectric response is written as (2.3). Solving for the fields in a planar Au mirror with plane wave illumination use (2.3), where the second term is zero with normal illumination, leads to the force density and hence a pressure that is very close to that from (2.1) with $|\Gamma| = 1$. This pressure on a planar surface thus provides a good

reference for the results we present. While (2.1) provides a reasonable description for the force on a planar surface with no transmission, (2.3) allows the 3D structured material situation to be treated, where both the cross and gradient terms contribute to the pressure with a structured material.

3.2 Design and Simulation

We use a 50 nm silicon nitride (SiN) membrane coated with 50 nm Au on both sides and guidance from a 2D numerical (finite element method) field solution of the periodic geometry in Fig. 3.1(b) [25], with an incident plane wave having a free space wavelength of 1070 nm. The force density in the material from (2.3) is integrated over the unit cell area ($x - y$ plane), and the pressure is obtained by normalizing with the invariant z-direction and the unit cell width (Λ). Two degrees of freedom were considered, the period (Λ) and the slot width (W). An elliptical slot taper (a consequence of the fabrication process) was used with an axial ratio of $\sqrt{3}$, the Au thickness divided by the taper width at the SiN interface, obtained from a fit to scanning electron micrograph (SEM) image data for fabricated structures, so the slot width at the top is larger than W by this amount. The dielectric constant for Au assumed is $-49.05 + i3.65$ [26], and that for the SiN membrane was obtained as 3.94 from an ellipsometer measurement.

The simulated field and optical force densities for three geometries that were fabricated are shown in Fig. 3.2, and W and Λ (shown in Fig. 3.1(b)), and the calculated pressure, P, for each are given in the caption. The plane wave (E_x, H_z) normally incident from the top has a power density of 318 MW/m^2, roughly 1 mW over a 1 μm radius circle. Figures 3.2(a)-(c) show a strong pushing force (Strong Push) situation (25.7 N/m^2) in the direction of the incident Poynting vector, Figs. 3.2(d)-(f) a strong pulling force (Strong Pull, -20.2 N/m^2), and Figs. 3.2(g)-(i) a weak pushing (Weak Push) force (3.26 N/m^2). The corresponding calculated pressure on the planar Au-SiN-Au film is 2.11 N/m^2 and on a perfect mirror is 2.12 N/m^2. The dissi-

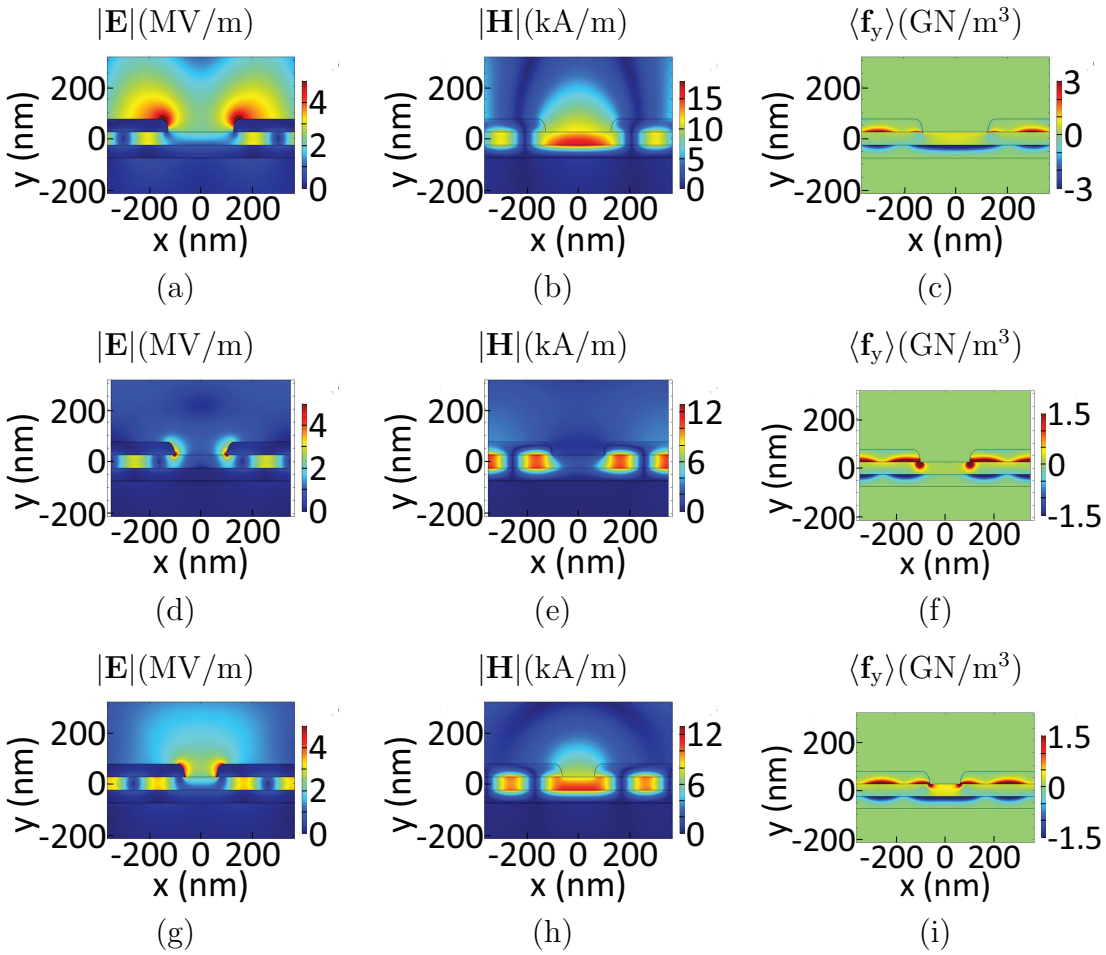

Fig. 3.2. Simulated fields and force densities for the periodic slot structure of Fig. 1(b): (a)-(c) Strong Push, $\Lambda = 966.4$ nm, $W = 250$ nm, $P = 25.7$ N/m^2; (d)-(e) Strong Pull, $\Lambda = 692.2$ nm, $W = 200.4$ nm, $P = -20.2$ N/m^2; (g)-(h) Weak Push, $\Lambda = 886$ nm, $W = 124$ nm, $P = 3.26$ N/m^2. The slot taper was determined according to SEM data from fabricated samples. The power density for the 1070 nm plane wave is 318 MW/m^2, corresponding to 1 mW over a 1 μm radius circle.

pated power density from optical absorption calculated in each case is: 227.9 MW/m^2 (Strong Push), 141.8 MW/m^2 (Strong Pull), and 143.9 MW/m^2 (Weak Push). The planar surface power dissipation is 22.6 MW/m^2. The intent was that the weaker pushing force case to be similar in magnitude to the planar case, and to be substantially smaller than those for the strong pushing and pulling structures. Numerical convergence studies based on element size refinement and slight rounding of the corners ensured the accuracy of the solutions for both the fields and the force densities. There is a metal-insulator-metal (MIM) waveguide mode established involving the Au and SiN interfaces that produces rather symmetric and competing force densities. A resonant surface wave at the Au-SiN interface at the bottom of the slot, clear in Fig. 3.2(b), provides the major pushing force, as is evident in Fig. 3.2(c). This phenomenon, with the relatively wide slot width, differs from the vertical MIM cavity array that produces an enhanced pressure [24]. The primary contribution to the pulling force is in the neighborhood of the Au slot, near the SiN surface, as Figs. 3.2(d) and (f) show for the field and force density, respectively. In this case, the scattered fields have been adjusted (by varying W and Λ) to produce a total field that imparts a net negative force. On the contrary, tractor beams pulling beads operate by control of the incident beam [28], although of course it is the total field also that imparts the force. The weak pushing force described in Fig. 3.2(i) results from competition between pushing and pulling forces.

We understand enhanced optical pressure, identified as a magnitude greater than $2S/c$, where S is the incident Poynting vector magnitude and c is the speed of light in vacuum, as being based on the excitation of resonances in the material. In the situations treated, the surface plasmon waves resonate. By controlling the geometry variables, the character of the fields and their resonances regulate the force density hence the pressure.

3.3 Fabrication

The slot arrays were formed in an Au coating on a SiN membrane (50 nm, Norcada, Inc.). The suspended square membrane had dimensions of 500 μm $\times$ 500 μm and was supported from four sides on a Si frame of thickness 200 μm. Gold of thickness 50 nm was deposited on both sides of the membrane using an electron-beam evaporator (CHA), following deposition of a 5 nm layer of titanium for adhesion. Thus, for practical purposes, a three-layered symmetric membrane structure made of Au-SiN-Au was formed. Focused Ion Beam (FIB) milling (FEI Nova 200) was used for fabrication of the slots on the bottom, recessed side of the structure (with a 10 pA current). Three periodic slot array structures were milled near the center of the membrane with nominal dimensions corresponding to those used in the simulations in Fig. 3.2 and measured dimensions indicated in the caption of Fig. 3.3. The SEM image for these slot arrays is shown in Fig. 3.3(a). A fourth symmetric location was used for the planar deflection data. A magnified image of the large pushing force structure (top left of Fig. 3.3(a)) is shown in Fig. 3.3(b). Images from an SEM (Hitachi S-4800) with an edge detection method that defines the edges from the local maximum gradient of the image intensity [29] provided precise geometry information for the fabricated structures for analysis and extraction purposes.

3.4 Experiment

The membrane was mounted on a glass slide with a hole to allow the 1070 nm force laser beam to directly illuminate the structured Au surface formed on the back of the membrane. As Figure 3.4(a) illustrates, the intensity modulated (mechanically chopped at 220 Hz) force laser illuminated the bottom, structured side of the membrane and a 640 nm sensing laser, positioned on the other (non-patterned) side and directly opposite the force laser, allowed the membrane deflection to be monitored by measurement of the current from a four quadrant detector. The specifics of the experiment are shown in Fig. 3.4(b). Measurement of the deflection signal at

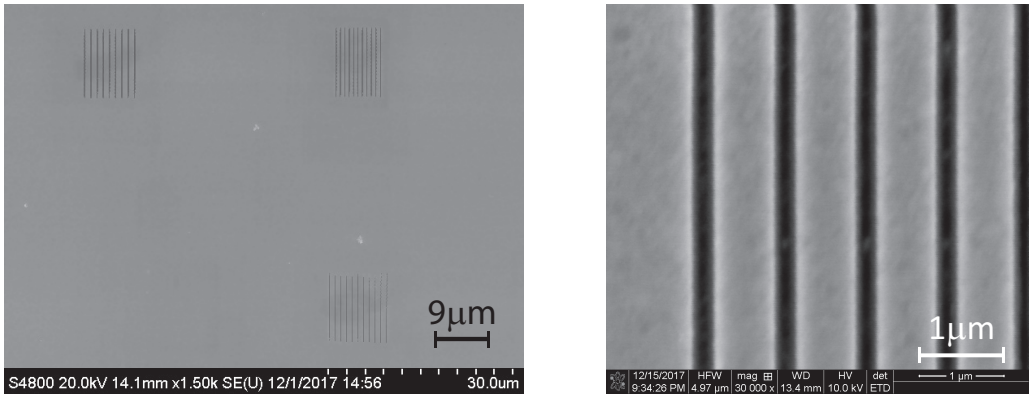

(a) (b)

Fig. 3.3. (a) The three slot arrays with an enhanced optical force: Strong Push, top left; Strong Pull, top right; and Weak Push, bottom right. SEM image data indicates: all slots have a length of 11.5μm; for the Strong Push structure, 9 slots with $W = 250 \pm 2.2$ nm, $\Lambda = 966.4 \pm 7.7$ nm; for the Strong Pull structure, 11 slots with $W = 200.4 \pm 3.4$ nm, $\Lambda = 692.2 \pm 7.3$ nm; and for the Weak Push structure, 11 slots with $W = 124 \pm 3.3$ nm, $\Lambda = 886 \pm 9.8$ nm. (b) A higher magnification SEM of the Strong Push slot array.

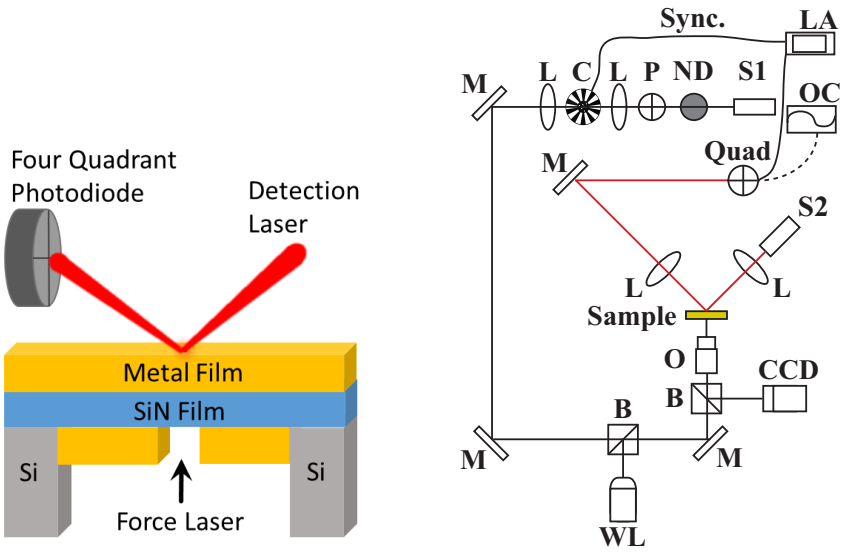

Fig. 3.4. (a) The measurement of deflection uses a quadrant detection system, allowing monitoring of the deflection due to the chopped 1070 nm force laser (polarized with magnetic field out of the page). (b) Schematic for the experiment. S1: 1070 nm CW fiber force laser (IPG photonics YLR-10-AC); S2: 640 nm sensing laser (Coherent StingRay); Quad: Quadrant photodiode (OSI Optoelectronics SPOT 9D-MI) with 640 nm bandpass filter and amplifier (OnTrak OT-301); OC: Oscilloscope; LA: Lock-in amplifier; ND: Neutral density filter; WL: White light source; P: Polarizer; C: Chopper; O: Objective lens; M: Silver mirror; B: Beam splitter; L: Lens; CCD: charge coupled device (camera). The membrane structure location was adjusted using a computer-controlled X-Y stage.

the chopping frequency with a lock-in amplifier removes any deflection bias due to the sensing laser. By calibrating to a known displacement with a piezoelectric stage (Thorlabs PE4), we determined that the sensitivity of the lock-in amplifier led to a displacement accuracy of 0.35 nm, setting the lower bound for the results we show.

3.5 Results and Optical Force Extraction

The data we present is from a single set of experiments with the slot arrays formed on the same membrane. Using a force laser power of 1 mW, we scanned the membrane

to obtain the deflection as a function of incident laser position on the membrane, obtaining the lock-in amplifier results shown in Fig. 3.5. This data allowed location of the center of the slot arrays based on the local maximum deflection. With the center of the slot arrays determined, we measured the total deflection with illumination at the center of each slot array and the symmetric planar point, as a function of incident laser power. The deflection direction information from the lock-in amplifier phase data was verified at the four symmetric positions with an oscilloscope. The solid circle points in Fig. 3.6(a) show the measured (total) deflection and the dotted lines are a least mean square error fit for optical powers less than 1 mW, selected so that all of the data is in the small signal, linear regime (with respect to force laser power). The dotted lines are treated as the measured data for the three slot arrays and the planar surface. All four measurement locations on the membrane have the same deflection direction, towards the sensing laser side (and in the direction of the incident force laser). The total deflection in Fig. 3.6(a) for the Strong Push case is largest, followed by the Weak Push, Strong Pull, and, far smaller, the Planar case. The Strong Pull total deflection is less than the Weak Push because the optical force is in the opposite direction to the thermally-driven deflection. The measurement error bars (that are more pronounced in the expanded view) were determined based on 100 measurements with the lock-in amplifier (10 ms integration time for each datum and a total duration of 1 s), and are found to be negligible for our purposes.

The total deflection in Fig. 3.6(a) has contributions from both the direct optical force and heating. In the small displacement regime, the total deflection is linearly related to optical force and heating and can be described as a superposition of direct optical deflection and thermally-driven deflection. Both terms in (2.3) contribute to the direct optical force. An additional force contribution is needed to describe thermally-driven deflection, which is a result of optical absorption. We generate the simulated optical force from (2.3) and the dissipated power from optical absorption for each slot structure and the planar membrane using the respective numerical field solutions. Fitting parameters are used to relate the calculated optical force to de-

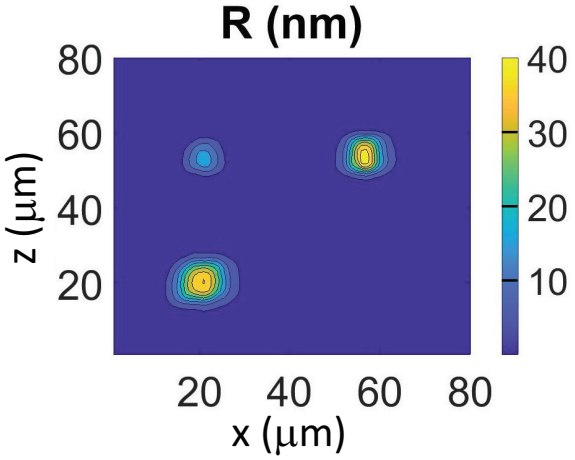

Fig. 3.5. Scanned membrane deflection magnitude (R) as a function of incident laser position with 1 mW force laser power. The location of the three slot arrays is clearly visible. The orientation of the three slot arrays differs from that in Fig. 3.3(a) because the sensing laser is on the opposite side of the membrane to the slots and the perspective of the SEM image.

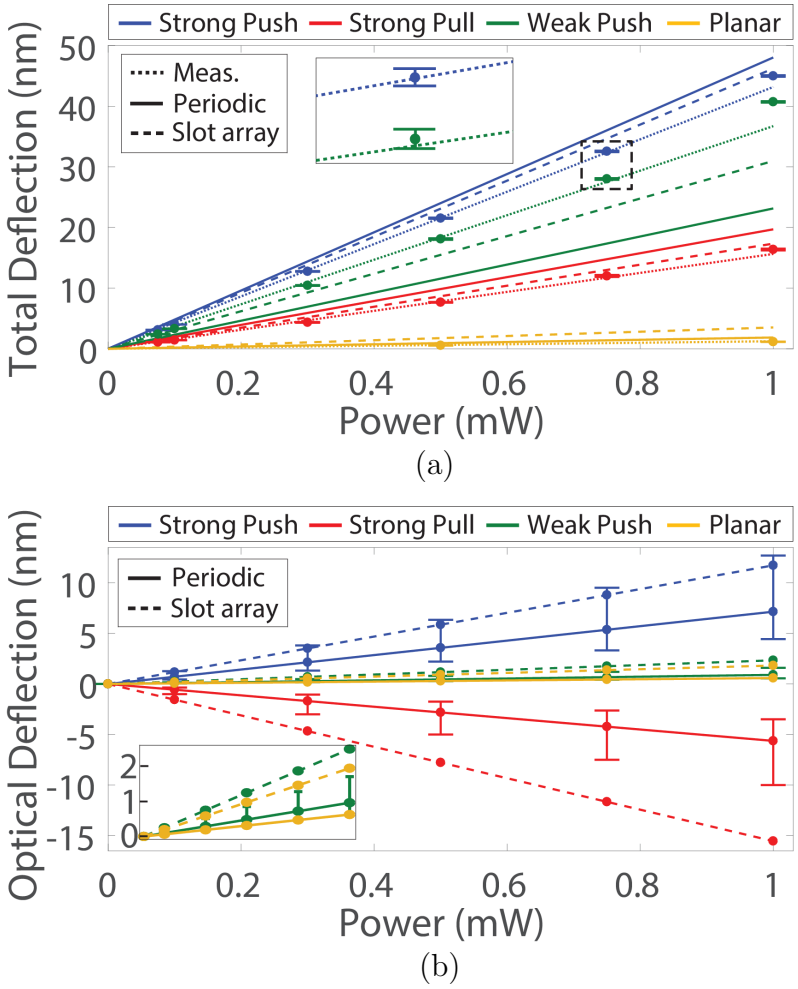

Fig. 3.6. (a) Measured (solid circles) and fitted and predicted (lines) total deflection as a function of incident laser power: enhanced pushing force (blue), enhanced pulling force (red), weak pushing force (green), and planar surface (yellow). Inset: enlargement of the dashed square region showing measurement error bars. Dotted: fits to the measured data; dashed: fits from a simulation with a Gaussian beam incident on each slot array; and solid: fits from a simulation with plane wave illumination of the corresponding periodic structures using the measured mean slot width and period. (b) Extracted optical deflection: dashed lines are from the exact slot array structures; solid lines are from the periodic structure simulations. The error bars describe sensitivity to structure using the means and standard deviations of the slot arrays from the SEM images (and are not the extraction errors). The inset shows an expanded scale data. The blue curves for a large pushing force show about an order or magnitude increase in pressure relative to the planar surface (yellow).

flection, α m/N, and the thermal dissipation to deflection, β m/W, resulting in a decomposition of the total deflection as $\mathbf{D} = \alpha\mathbf{F} + \beta\mathbf{T}$. Here, $\mathbf{D}$ is a vector of measured total displacements (the data for the three slot array structures and the planar case), $\mathbf{F}$ is a vector whose entries are the corresponding simulated optical forces from (2.3), and the vector $\mathbf{T}$ contains the simulated total dissipated power for each. The first term ($\alpha\mathbf{F}$) presents the deflection due to the optical force and the second term ($\beta\mathbf{T}$) that from optical absorption and hence heating. We use the dotted line fits in Fig. 3.6(a) to form $d\mathbf{D}/dP_o$ (a 4×1 vector), with P_o the variable force laser power, and then a least squares fit to estimate a single α and β for $d\mathbf{F}/dP_o$ and $d\mathbf{T}/dP_o$, respectively, that hold for all structures. The accuracy of this procedure is clear in predicting all experimental data, as shown in the deflection results of Fig. 3.6(a).

Figure 3.6(a) shows the results with two modeling approaches: a simple 2D periodic structure assumed for each slot array with plane wave illumination (solid), and a more accurate 3D Gaussian beam illumination of each slot array with a sequence of 2D slice solutions accounting for the beam profile along the length of the slots (dashed). The fields and force densities for each finite-width structure with a Gaussian incident field ($1/e$ field at a half-width of 7μm) was found to have similar key features to the 2D periodic case with plane wave illumination. The 2D slice approximation of the 3D solution was investigated by calculating the 3D force and dissipation on a planar (Ai-SiN-Au) surface by comparing with results from a superposition of 2D slices, and found to be satisfactory. The simulated results use the experimentally-derived α and β to relate calculated force and dissipation, respectively, to displacement. The simulated total deflection results using the periodic assumption (with the mean width and period of each array) compare favorably with those for each slot arrays with Gaussian beam illumination. All simulated results in Fig. 3.6(a) are sufficiently close to the measured data to make conclusions regarding extracted optical force deflection and related enhancement of the pressure.

The extracted optical deflection results as a function of incident optical power are shown in Fig. 3.6(b). The dashed lines are the results using the more accurate

slice model with the measured Gaussian beam profile. The mean values of each slot width and separation for each array were obtained from the SEM images and used to obtain the simulated results (with the extracted α and β). The substantial differences between the large pushing force and pulling force deflections and the planar results represent the force enhancement. In order to appraise sensitivity of the extraction to geometry variations, we pursued a statistical study, and those results are shown by the solid lines in Fig. 3.6(b) that have associated error bars. It should be emphasized that the resulting error bars are not the errors in determining the slot array parameters, but are an indication of the sensitivity of the method for determining optical force deflection to gross variations in the geometry, should there have been factors of which we were unaware. From the SEM images, we obtained a mean and a standard deviation for each array slot width and period (see the caption of Fig. 3.3). Based on the geometry means and the means plus and minus the standard deviations, we calculated the optical force and power dissipation and repeated the least square fitting process with all the combinations of slot widths and separations for the different sets of slots, using the simple plane wave model. We determined the standard deviations of the fitted optical deflections and plot these as the error bars in Fig. 3.6(b). The error bars are asymmetric because the points and lines were determined using the geometry's means, and the means from the statistical treatment are not identical. Note that even with this rather artificial and extreme set of variations in the extracted optical deflection, all results in Fig. 3.6(b) are distinct and clearly demonstrate an increase in deflection based upon slot structure, relative to the planar case. Importantly, Fig. 3.6(b) shows a force on the structured Au film, in the case of the large push force (blue), that is approximately an order of magnitude higher than that on the planar Au surface (yellow).

3.6 Conclusion

We have demonstrated an enhanced optical force on a metallic surface that depends on the nanostructured features. The increase in optical pressure therefore results from optical field interaction with the material in the third dimension. The general principle is that an asymmetric cavity-enhanced field increase, associated with a resonance, leads to an increase in the force density within the material and hence to a substantial increase in the total force, relative to the planar case. Control of the scattered field in the structured material can regulate both the force magnitude and direction, and allow a negative pressure. The interplay between material structured at the nanometer-scale and optical force will have substantial consequences in applications that include all-optical communication, remote actuation, propulsion, and biophysics. For example, in all-optical communication, optical signals could be used to move a structure that would then select a different optical (network) path [30,31]. Remote actuation would be enhanced by greater sensitivity and control of the force direction, both of which might benefit cavity cooling [32,33]. Regulation and enhancement of the optical force should prove interesting in the field of cavity optomechanics [34, 35]. Also, by structuring beads used in optical tweezer experiments related to biomolecules, more control during experiments to evaluate the influence of force and torque may be possible with patterned beads [7]. Finally, there has also been interest in thermomechanical structures, where light is used to heat and deform metal films [36].

3.7 Contribution

Li-Fan was responsible for the design and simulation, experiment, and data analysis with great assistant from Anurup Datta, who worked with Prof. Xianfan Xu, on the membrane fabrication and also the experiment.

4. ENHANCED OPTICAL PRESSURE WITH ASYMMETRIC CAVITIES[†]

In this chapter we theorize and explain that asymmetry in a one-dimensional optical Fabry-Perot optical cavity is shown to produce a large net pressure, the total on the two mirrors. Consequently, asymmetric cavity structures that are formed in this manner can experience a net force that is greater than that resulting from the excitation light illuminating a perfect mirror. The conditions for this to occur are a modest quality factor regime, where some influence of the cavity is needed, but when the quality factor becomes very large the enhancement diminishes. This result is used to illustrate how structuring a metal surface, thereby forming a plasmonic cavity, can substantially increase the optical pressure over that possible with a planar interface. It is shown that the force on one mirror in an asymmetric arrangement can be increased relative to the other. Importantly, the sum of the pressures on both mirrors increases through asymmetry and with quality factor, while adhering to conservation of energy. Using cavity quality factor as a measure, the one-dimensional Fabry-Perot cavity pressure results are related to pressure enhancement with a structured metal surface where a different type of mode in an asymmetric cavity is excited, the lowest order metal-insulator-metal surface plasmon mode. In principle, an optical cavity or cavity array formed with any material should display this enhanced pressure phenomenon. The length scale of the resonant structures for visible light can be as small as a few tens of nanometers, in the case of metals. With this understanding guiding the design of structured metallic and dielectric materials, a many-fold increase in pressure over

[†] This work is published as
Y. -C. Hsueh, L. -F. Yang, and K. J. Webb, "Enhanced optical pressure with asymmetric cavities," *Phys. Rev. B*, 99(4), 045437, 2019 (Ref. [16])

that on a perfect mirror is possible. Consequently, the relatively weak optical force can become more effective in a variety of scientific and technological applications.

4.1 Introduction

The force density in homogenized media can be obtained from the field solution, and this leads to a means to calculate the force on a medium [12, 23], the pressure on a slab [37, 38], and with photonic crystal mirrors [39]. With such an approach involving a numerical solution for the fields in the material, leading to the force density and hence pressure, the possibility of increasing the pressure by more than an order of magnitude over $2S/c$ from (2.1) with a nanostructured Au surface has been presented [24], introduced in Chapter 2. This result could be profoundly important in applications, but the physical basis of the effect has remained unclear. Here, we present an understanding based on results for an asymmetric 1D Fabry-Perot cavity and explain how the the sum of the pressures on each mirror can exceed that on a perfect mirror. This cavity mode basis leads to a means to achieve pressure enhancement with a variety of dielectric and metallic materials for remote control, propulsion, and cavity optomechanics applications. The resulting change in the mathematical picture of pressure [3] should therefore provide a basis for new directions in optomechanics for the physical sciences.

We explain optical pressure enhancement on a surface by considering the mirror pressures in the 1D Fabry-Perot cavities shown in Figs. 4.1(a) and (b), which we relate to cavity Q and the metal-insulator-metal (MIM) cavity mode in Figs. 4.1(c) and (d), all in a free space background. Figure 4.1(a) shows a symmetric cavity containing two identical slab mirrors (M_1 and M_2) with thickness t, and a cavity length d, defined as the mirror separation. Figure 4.1(b) shows an asymmetric cavity with M_1 having thickness t and the semi-infinite M_2 placed a distance d away from M_1. Figure 4.1(c) shows a nanostructured slot cavity array in metal and the profile of each slot is shown in Fig. 4.1(d). With an incident field having H_z, the lowest order MIM

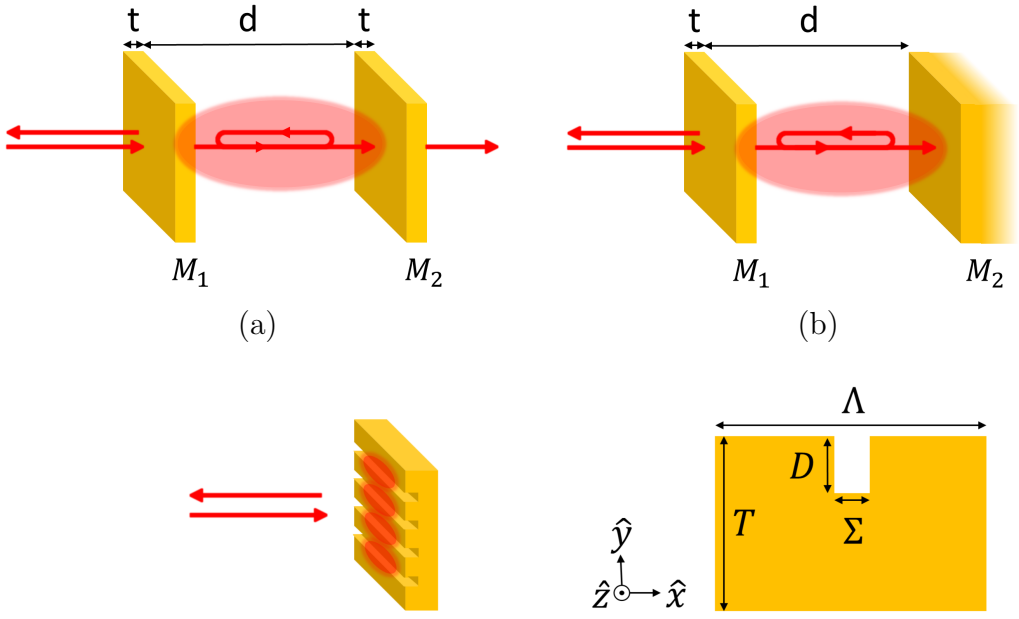

Fig. 4.1. Optical cavities that enhance the radiation pressure. (a) A symmetric Fabry-Perot cavity. The mirrors M_1 and M_2 are two identical slabs with thickness t separated by d. (b) An asymmetric Fabry-Perot cavity. M_1 is a slab with thickness t and M_2 is a semi-infinite mirror placed d away from M_1. (c) A nanostructured slot cavity array in a metal. (d) Profile of the nanostructured slot cavity in (c). A normally-incident plane wave of wavelength 633 nm and Au with artificially adjusted loss are assumed, as described in Table 4.1.

Table 4.1.
The cavity mirror material parameters used in the calculations related to Figs. 4.1(a) and (b). Nomenclature: symmetric Fabry-Perot (SFP), cases 1 (SFP1) and 2 (SFP2), as in Fig. 4.1(a); asymmetric Fabry-Perot (AFP), cases 1-3, as in Fig. 4.1(b). The dielectric constant assumed for Au is $\epsilon_{Au} = -11.82 + i1.23$ at a wavelength of 633 nm, and in all cases, $\epsilon'_{\mathrm{M1}} = \epsilon'_{\mathrm{M2}} = -11.82$. The imaginary part of the dielectric constant for each mirror, ϵ''_{M1} and ϵ''_{M2}, is varied as indicated to adjust the confinement and dissipation in the cavities.

<table>
<tr><td></td><td>t_{M_1}</td><td>ϵ''_{M_1}</td><td>t_{M_2}</td><td>ϵ''_{M_2}</td></tr>
<tr><td>SFP1</td><td>30 nm</td><td rowspan="4">0, 0.1, 0.2, $\cdots$, 1 and 1.23 ($\Im\{\epsilon_{Au}\}$)</td><td colspan="2" rowspan="2">Same as M_1</td></tr>
<tr><td>SFP2</td><td>50 nm</td></tr>
<tr><td>AFP1</td><td>30 nm</td><td rowspan="3">Semi-infinite</td><td rowspan="2">1.23 ($\Im\{\epsilon_{Au}\}$)</td></tr>
<tr><td>AFP2</td><td>50 nm</td></tr>
<tr><td>AFP3</td><td>50 nm</td><td></td><td>0.1</td></tr>
</table>

waveguide mode (E_x, E_y, H_z) can be excited, by virtue of the metal dielectric constant ($\epsilon = \epsilon' + i\epsilon''$ with $\epsilon' < -1$, assuming a free space background) [40]. The coupled surface plasmon waveguide mode has a wavelength that reduces with decreasing slot width (Σ), allowing for resonant cavities in gold (Au) where the slot depth (D) and Σ are just a few tens of nanometers. The cavity in Fig. 4.1(d) has differing reflection coefficients at the top and bottom of the slot, resulting in asymmetry. We present radiation pressure simulation results for 1D cavities in Figs. 4.1(a) and (b) and use these to build physical insight into the influence of structures like Figs. 4.1(c) and (d) to enhance the pressure.

4.2 Field Solution and Quality Factor for Cavity Pressure

The field solutions in the Fabry-Perot cavities in Figs. 4.1(a) and (b) can be solved analytically. and we do so for excitation with a single, normally incident plane wave from the left, allowing the force densities in the mirrors and hence the pressure to be obtained. Each cavity is a 1D multilayer structure that can be treated using an established method [41]. A convenient way to do this is to write the impedance transformation between boundaries m and $m+1$ as

$$Z_m = \eta_m \frac{Z_{m+1} - i\eta_m \tan k_m l_m}{\eta_m - iZ_{m+1} \tan k_m l_m}, \quad \text{with} \quad m = 4, 3, 2, 1 \tag{4.1}$$

where η_m, k_m, and l_m are the characteristic impedance, phase constant, and thickness, respectively, of the mth region, initialized by $Z_4 = \eta_0$, the free space wave impedance on the right side of M_2 in Fig. 4.1(a). The electric field reflection coefficient on the left boundary in Fig. 1(a) is $S_{11} = (Z_1 - \eta_0)/(Z_1 + \eta_0)$, where we have used scattering parameter notation. The total electric and magnetic fields at Boundary 1 are thus $E_1 = (1 + S_{11})E_0$ and $H_1 = (1 - S_{11})E_0/\eta_0$, where E_0 is the incident electric field phasor. Then, the electric and magnetic fields everywhere in this 1D multilayer structure can be calculated from

$$\begin{bmatrix} E_{m+1} \\ H_{m+1} \end{bmatrix} = \begin{bmatrix} \cos k_m l_m & i\eta_m \sin k_m l_m \\ i\eta_m^{-1} \sin k_m l_m & \cos k_m l_m \end{bmatrix} \begin{bmatrix} E_m \\ H_m \end{bmatrix}, \quad \text{with} \quad m = 4, 3, 2, 1, \tag{4.2}$$

initialized by E_1, H_1. The field solutions allow the stored energy W, the cavity Q, the force densities in the mirrors and hence the pressure to be obtained. The fields in the asymmetric Fabry-Perot cavity shown in Fig. 1(b) can be likewise found. We choose reflected fields rather than those transmitted because some cavities of interest have no transmission. The force density expression we utilize here, originally from Einstein and Laub [13], is shown in (2.2) with the time-averaged form in (2.3).

We define the time-averaged force density due to the first term in (2.3) as $\langle \mathbf{f}_{\mathrm{R}} \rangle$, where the nomenclature implies that this is the radiation pressure for a planar surface with normal incidence, the usual mirror picture, and the other term due to the gradient of the field as $\langle \mathbf{f}_{\mathrm{G}} \rangle$. We note that application of (2.3) for normally incident light on a planar Au mirror and integration over depth produces a pressure for visible wavelengths that is very close to $2S/c$.

We relate the radiation pressure to the cavity Q for the 1D cavities in Figs. 4.1(a) and (b). With the linear and isotropic relationships $\mathbf{D} = \epsilon_0 \epsilon \mathbf{E}$ and $\mathbf{B} = \mu_0 \mathbf{H}$, in frequency domain and where $\mathbf{D}$ is the electric flux density and $\mathbf{B}$ the magnetic flux density, it is possible to separate electromagnetic field energy into stored and lost components [42]. Under the assumption that dispersion can be neglected, so $\partial\epsilon/\partial\omega = 0$, the time-averaged stored energy surface density ($\mathrm{J/m^2}$) is

$$W = \frac{1}{4} \int_l \left[\epsilon' \epsilon_0 |E(\mathbf{r})|^2 + \mu_0 |H(\mathbf{r})|^2 \right] \mathrm{d}l, \tag{4.3}$$

where l is the spatial variable perpendicular to the mirrors. Likewise, the time-averaged power dissipation surface density ($\mathrm{W/m^2}$) is

$$P_{\mathrm{d}} = \frac{\omega}{2} \int_l \epsilon_0 \epsilon'' |E(\mathbf{r})|^2 \mathrm{d}l. \tag{4.4}$$

The integrations in (4.3) and (4.4) are over the mirrors and the intervening space (free space in the situations of Figs. 4.1(a) and (b)), and for $\mathrm{M_2}$ in the asymmetric cavity case, the integral in that mirror is over 20δ, with δ the skin depth (e^{-1} of the field at the surface).

The Q can be decomposed into unloaded (accounting for loss within the cavity, Q_{U}) and loaded (describing the radiative loss contribution, Q_{L}) as

$$\frac{1}{Q} = \frac{1}{Q_{\mathrm{U}}} + \frac{1}{Q_{\mathrm{L}}}, \tag{4.5}$$

where

$$Q_{\mathrm{U}} = \omega_0 \frac{W_0}{P_{\mathrm{d}}} \quad \text{and} \quad Q_{\mathrm{L}} = \omega_0 \frac{W_0}{S_{\mathrm{r}} + S_{\mathrm{t}}}, \tag{4.6}$$

with ω_0 the resonant circular frequency, W_0 the total (electric plus magnetic) energy in the cavity at resonance from (4.3), P_{d} the power dissipated within the cavity at resonance from (4.4), and S_{r} and S_{t} the reflected and transmitted Poynting vector magnitudes, respectively, at resonance. With high cavity finesse and use of a Lorentzian line model [43, 44],

$$1 - |S_{11}(\omega)|^2 = \frac{1 - |S_{11}(\omega_0)|^2}{1 + 4\frac{(\omega_0 - \omega)^2}{\Delta\omega^2}}, \tag{4.7}$$

and an estimate of Q is

$$Q_\omega = \frac{\omega_0}{\Delta\omega}, \tag{4.8}$$

where $\Delta\omega$ is the half-power bandwidth and the subscript ω indicates this frequency response measure (with a high Q approximation). Measuring S_{11} and use of (4.8) to determine Q circumvents the need to artificially define cavity boundaries.

4.3 Pressure with a One-Dimensional Asymmetric Cavity

Figure 4.2 shows our pressure results for the 1D cavities of Figs. 4.1(a) and (b) at resonance. We designate symmetric (Fig. 4.1(a)) and asymmetric (Fig. 4.1(b)) Fabry-Perot cavity cases through the labels SFP and AFP, respectively. In all calculations, the magnitude of the Poynting vector of the normally incident plane wave (S_i) on the cavity is 1 W/m^2, and the free space wavelength is $\lambda_0 = 633$ nm. The mirror dielectric constants used are presented in Table 4.1 and based on Au. We vary only the material loss and thickness to adjust the confinement and dissipation in the

cavities. The shortest resonant cavity length was determined from the minimum $|S_{11}|$ as d is adjusted, and all results are for this condition. For the 1D cavities, only $\langle \mathbf{f}_{\mathrm{R}} \rangle$ contributes to the pressure. Positive pressure is in the direction of the wave vector for the cavity excitation and the excitation Poynting vector. Consequently, M_1 has positive pressure due to excitation and negative pressure due to the cavity field, and the latter dominates in the cases considered. The pressure on M_2 is always positive. Our central interest is in the sum of the pressures on the two mirrors.

Figure 4.2(a) shows the radiation pressure on M_2, P_{M_2}, as a function of Q, calculated from (4.5), with use of (4.6), and the cavity energy determined from (4.3) and the power dissipation from (4.4). The various symmetric (SFP) and asymmetric (AFP) cavity parameters are given in Table 4.1. The Q is adjusted by varying the loss in M_1 through $\epsilon''_{\mathrm{M}_1}$. Changing $\epsilon''_{\mathrm{M}_1}$ has an impact on the coupling between the incident wave and the cavity, so both Q_{U} and Q_{L} are varied, and the stored energy in the cavity changes. The increase in P_{M_2} with increasing Q can be understood from the pressure presented by Maxwell [3] in (2.1) with $|\Gamma| \sim 1$ and the increasing forward power density (S_{f}). A fit (orange line) in Fig. 4.2(a) makes the linear relationship between pressure and Q clear. Figure 4.2(b) shows P_{M_2} as a function of Q_ω, estimated from (4.8), which has a nonlinear relationship to pressure. However, the general trend between pressure and both Q and Q_ω are consistent. The nonlinear character in Fig. 4.2(b) appears at lower values of Q_ω and can be attributed to the breakdown of the high-Q approximation. With high Q_ω, the results in Fig. 4.2(b) still differ a little from those in Fig. 4.2(a) because the cavity boundaries were (artificially) described at the outside of the mirror surfaces in determining both W_0 and Q (in Fig. 4.2(a)), while use of the reflection coefficient in (4.7) in determining Q_ω from (4.8) did not require a cavity boundary to be defined. We conclude then that Q_ω provides a suitable measure to investigate cavity mirror pressure.

Figure 4.2(c) shows the net pressure on M_1 and M_2, $P_{\mathrm{M}_1} + P_{\mathrm{M}_2} = P_{\mathrm{M}_1+\mathrm{M}_2}$, for SFP2 and AFP3, the higher Q examples of symmetric and asymmetric cavities, respectively. When a symmetric cavity is resonant, the forward and backward waves within the

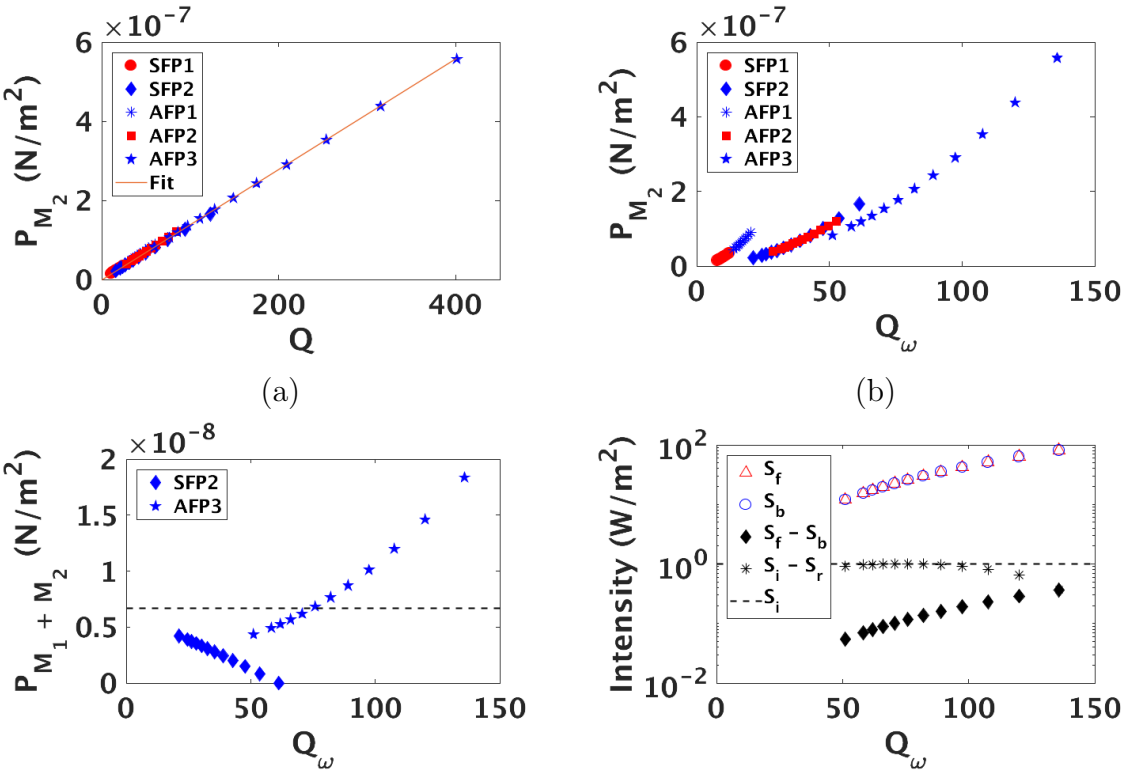

Fig. 4.2. (a) P_{M_2} on M_2 as a function of Q from (4.5), with a linear fit (orange line) for examples of symmetric and asymmetric Fabry-Perot cavities with the parameters given in Table 4.1. (b) P_{M_2} as a function of Q_ω from (4.8). (c) Net pressure, $P_{M_1+M_2}$, on M_1 and M_2 as a function of Q_ω. The dashed line shows the value of the maximum pressure on a perfect mirror when the magnitude of the incident power density (S_i) is 1 W/m^2. A resonant asymmetric cavity can support larger pressure enhancement than a perfect reflecting (anti-resonant) surface. (d) Forward (S_f) and backward (S_b) power density for the asymmetric cavity AFP3 (overlapping on this scale), along with the difference ($S_f - S_b$), in comparison with the incident (S_i) and the net incident ($S_i - S_r$) power densities. As Q increases due to reduced loss in M_1, $S_f - S_b$ approaches $S_i - S_b$. This result establishes conservation of energy.

cavity have approximately the same amplitude. Therefore, for the symmetric cavity, P_{M_1} (< 0, the sum of the excitation light pressure, which is positive, and the much larger negative cavity pressure) is almost the same as P_{M_2} (> 0), but in the opposite direction and hence a negative number, causing $P_{\mathrm{M}_1+\mathrm{M}_2}$ to be small. This can be observed from the blue diamond symbols in Fig. 4.2(c), where the total pressure becomes small as Q_ω increases. On the other hand, with the asymmetric mirror arrangement of Fig. 4.1(b), P_{M_2} is slightly larger than P_{M_1}, leading to an increasing $P_{\mathrm{M}_1+\mathrm{M}_2}$ with increase in Q_ω over the range considered, as evidenced by the star symbols in Fig. 4.2(c). The dashed line in Fig. 4.2(c) shows the maximum pressure on a perfect mirror based on (2.1) when $S = 1$ W/m^2 and $\Gamma = 1$. From the AFP3 case in Fig. 4.2(c), given by the blue stars, it is clear that $P_{\mathrm{M}_1+\mathrm{M}_2}$, enhanced by the cavity Q, can exceed the maximum pressure on a perfect mirror ($2S/c$) by a factor of three (with the same power density incident on the cavity).

Figure 4.2(d) shows the power flow for the asymmetric cavity case of Fig. 4.2(c), AFP3. Conservation of energy requires that the difference between the forward and backward Poynting vector magnitudes in the cavity and between the mirrors ($S_\mathrm{f} - S_\mathrm{b}$) be less than or equal to (when the mirrors have no dissipative loss) the net power density exciting the cavity ($S_\mathrm{i} - S_\mathrm{r}$). Figure 4.2(d) shows that this is the case and energy is conserved. The $S_\mathrm{f} - S_\mathrm{b}$ curve approaches $S_\mathrm{i} - S_\mathrm{r}$ with increasing Q because the loss in M_1 is being reduced. We can thus understand the enhanced net pressure ($P_{\mathrm{M}_1+\mathrm{M}_2}$) as being regulated by asymmetric cavity control of $S_\mathrm{f} - S_\mathrm{b}$ and cavity Q, while maintaining conservation of energy and momentum.

It is interesting to note from the results of Fig. 4.2 that, at the first resonance, $P_{M_1+M_2}$ is largest when the reflection coefficient at the left of M_1 ($|S_{11}|$) is a minimum. On the contrary, the maximum pressure based upon $S(1+|\Gamma|^2)/c = 2S/c$ occurs when the reflection coefficient is maximum. The idea that higher reflection produces larger pressure has led to the use of highly reflecting surfaces achieved with distributed Bragg reflectors or photonic crystals. Our results indicate, quite differently, that a

resonant asymmetric cavity can provide even larger pressure enhancement than the conventional limit.

To understand the pressure enhancement when the cavity supports even higher Q, we calculate the net pressure, $P_{M_1+M_2}$, for symmetric and asymmetric Fabry-Perot cavities with Q_ω larger than AFP3 in Fig. 4.2(c), finding the results in Fig. 4.3(a). The dielectric constants of M_1 and M_2 are fixed to be $\epsilon'_{M1} = \epsilon'_{M2} = -11.82$ and $\epsilon''_{M1} = \epsilon''_{M2} = 0.1$. We adjust thickness of M_1, t, to be $5, 10, 40, 50, 70, 80, 100, 130$ and 150 nm to gradually increase cavity quality factor, Q_ω. The symmetric cavities contain identical thicknesses of M_1 and M_2. In principle, the symmetric cavity pressure should approach the perfect mirror case, the dashed line in Fig. 4.2(c) when M_1 is very thick to obtain high Q. This can be observed from the diamond symbols. Note how $P_{M_1+M_2}$ increases to approach the dashed line and the perfect mirror situation, indicating the that internal cavity pressures cancel and the small cavity coupling results in close to a perfect mirror at M_1. For asymmetric cavities (star symbols), notice in Fig. 4.3(a) that $P_{M_1+M_2}$ has a value below the perfect mirror case and initially increases with increasing Q_ω, reaches a maximum, and then decreases to the perfect mirror value. When t becomes large and cavity Q is very high, the cavity behaves more like a symmetric cavity where the pressures on M_1 and M_2 due to S_b and S_f cancel. The net pressure for high Q approaches that from the excitation wave on a planar surface. We therefore learn by way of example and consideration of the underlying physical mechanism that there is a regime with modestly high Q where pressure enhancement with asymmetric cavities can occur.

4.4 Cavity Pressure with Maxwell's Picture

In Fig. 4.2 we show calculated results for the pressure from a force density stemming from work by Einstein and Laub [13] given in (2.3). Integration of the force density over the material and normalization to surface area led to the pressure. For the 1D cavity problem we treated and normal incidence, only the first term in (2.3) con-

tributes. On the other hand, a commonly used picture was proposed by Maxwell [3], where the radiation pressure is given by (2.1) when there is no transmission through the mirror.

We compare the pressures on M_1 and M_2 in Fig. 4.1(b), P_{M1} and P_{M2}, based on these two approaches, i.e., with use of (2.1) and (2.3). In applying (2.1) to M_1, we consider only the more significant pressure from the cavity field and hence neglect that due to the excitation field on this mirror. We choose AFP3 (the asymmetric cavity in Fig. 4.1(b) with the parameters given in Table 4.1) because of the larger pressure enhancement and higher Q among the Fabry-Perot cavity examples in Fig. 4.2. The results for P_{M1}, P_{M2} and the net pressure, P_{M1+M2}, for AFP3, are shown in Fig. 4.4. Changing the material in mirror M_1 produces a change in cavity Q and hence a change in the pressure. In Fig. 4.4, the black stars are from Maxwell's picture in (2.1) and the blue stars are calculated from (2.3).

We note that P_{M1} is in the opposite direction of P_{M2}. By using (2.1) for P_{M1}, we assume that M_1 provides high reflection and efficient absorption within the material. Therefore, the results have the assumption that no transmission occurs through M_1, causing a slightly larger P_{M1}. We can also observe the slight differences between the pressures calculated from two approaches in Fig. 4.4(b) due to the influence of the finite penetration (20δ, with δ the skin depth) into M_2 in forming the pressure from (2.3). These small differences are more evident for larger Q_ω because the scale is expanded in this regime and reduce with increasing accuracy for the integration of the force density. The use of (2.1) for M_1 produces higher P_{M1} and hence a lower estimate for the net pressure, P_{M1+M2}. This can be observed in Fig. 4.4(c) with increasing Q_ω. With an increase of Q_ω, the loss of M_1 reduces, causing the larger differences between the two approaches when we use (2.1) for M_1. However, the enhanced pressure beyond that on a perfect mirror can still be observed when we apply Maxwell's picture. Generally, for this 1D problem, we note the excellent agreement between the two approaches. Our conclusion is that either model would serve our purpose.

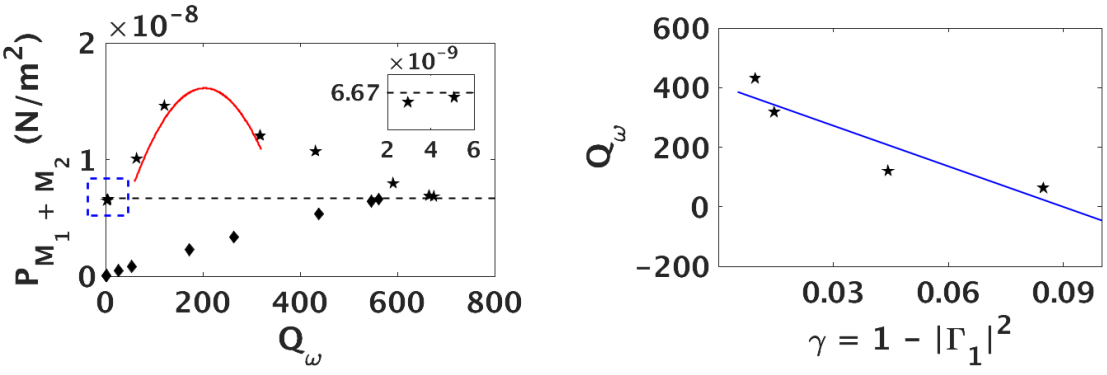

(a) (b)

Fig. 4.3. (a) The net pressure on M_1 and M_2, $P_{M_1+M_2}$, as a function of Q_ω for symmetric (diamonds) and asymmetric (stars) Fabry-Perot cavity having $\epsilon'_{M1} = \epsilon'_{M2} = -11.82$ and $\epsilon''_{M1} = \epsilon''_{M2} = 0.1$. We choose the thickness of M_1, t, to be $5, 10, 40, 50, 70, 80, 100, 130$ and 150 nm to regulate the cavity quality factor, Q_ω, in the regime where enhancement occurs and beyond. The sub-figure shows an expanded view of the dashed box region for small Q_ω. The dashed line shows the value of the maximum pressure on a perfect mirror when the magnitude of the incident power density (S_i) is 1 W/m^2. For symmetric cavities (diamonds), the total pressure increases with increasing Q_ω, and then approaches the perfect mirror case. For asymmetric cavities (stars), note that the total pressure dips below that for S_i incident on a perfect mirror for low Q_ω. These results show that there is a design region for pressure enhancement. When t becomes large, the cavity behaves more like a symmetric cavity where the pressures on M_1 and M_2 due to S_b and S_f approximately cancel. In this regime, the net pressure is roughly that from the excitation wave on a planar surface. The red parabola is from the local linear estimation for the asymmetric cavity data points with $t = 40, 50, 70$ and 80 nm and use of (4.16). (b) Calculated $Q_\omega(\gamma)$ with $\gamma = 1 - |\Gamma_1|^2$ (asymmetric cavity data points with $t = 40, 50, 70, 80$ nm). The blue line is a fit to all points, yielding $Q_\omega(\gamma) = a_n\gamma + b_n$ with $a_n = -4.5350 \times 10^3$ and $b_n = 407.3813$. With use of the point with $t = 50$ nm which shows the largest enhancement in (a) and the corresponding Q (blue star symbol with the second largest Q in AFP3) in Fig. 4.2(a), we find $Q = \beta Q_\omega$ with $\beta = 2.6073$. The a_n and b_n provide local a and b values in (4.16) and the resulting parabolic curve in (a). Note how well this local, linear picture (the red parabola) captures the pressure enhancement.

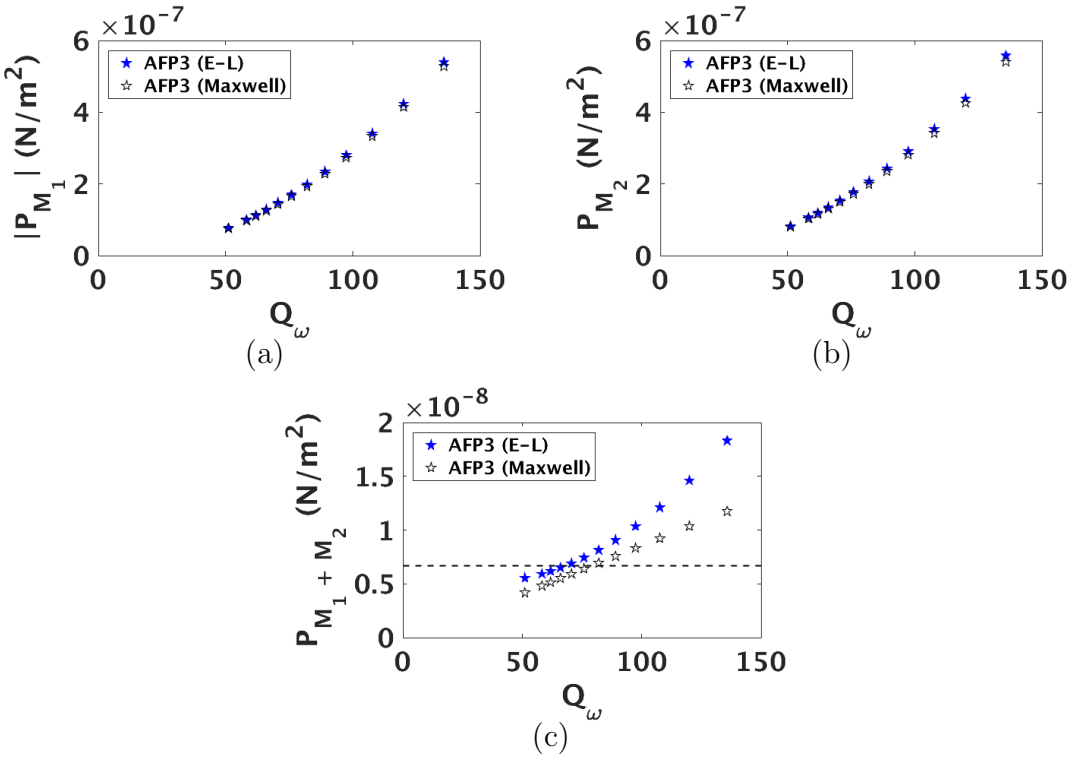

Fig. 4.4. The pressures on M_1 and M_2 in the cavity of Fig. 4.1(b) using the Einstein-Laub (2.3) and Maxwell (2.1) descriptions, with varying loss for M_1 (ϵ''_{M1}) and hence varying cavity quality factor, Q_ω. $\epsilon'_{M1} = \epsilon'_{M2} = -11.82$ is fixed for both mirrors and $\epsilon''_{M2} = 0.1$. (a) Radiation pressure on M_1 in Fig. 4.1(b), $|P_{M_1}|$, as a function of cavity quality factor, Q_ω, for the asymmetric Fabry-Perot cavity having mirror M_1 material properties described as AFP3 in Table 4.1. Varying the mirror material causes Q_ω to change and hence the pressure, and this relationship is presented. The black stars are estimated from Maxwell's picture in (2.1), assuming there is no transmission through the mirror. The blue star symbols are calculated from the integral of the force density within the scattering material using the Einstein-Laub description in (2.3). (b) P_{M_2} from Maxwell's picture in (2.1) (black stars) and from the Einstein-Laub force density description in (2.3) (blue stars). (c) The net pressure, $P_{M_1+M_2}$, from Maxwell's picture in (2.1) (black stars) and from the Einstein-Laub force density description in (2.3) (blue stars). The larger differences with increasing Q_ω between the two approaches comes from the assumption of no transmission for M_1. The dashed line shows the value of the maximum pressure on a perfect mirror when the magnitude of the incident power density is 1 W/m^2. The enhanced pressure can be observed in both approaches. Our conclusion is that both theories present essentially the same mirror pressure results.

To confirm that we have the correct field solutions, Fig. 4.5 plots the magnitudes of the electric and magnetic fields through the cavity for the three AFP3 examples with the largest Q ($Q_\omega = 135.84, 120, 107.67$ when $\epsilon''_{\mathrm{M}_1} = 0, 0.1, 0.2$, respectively) in Fig. 4.4 where there is significant pressure enhancement and high Q. The field values can be used to verify the corresponding power flow points in Fig. 4.2(d) and the pressure enhancement for this case. The magnitude of electric field in Fig. 4.5(a), (c) and (e) and magnetic field in Fig. 4.5(b), (d) and (f) indicate the quasi-even electric field and quasi-odd magnetic field solutions for the first resonant mode in the asymmetric cavity. These field solutions clearly satisfy the boundary conditions and hence represent both the unique and exact field solution for this particular situation. Consequently, the approximate pressures from (2.1) or the exact results from (2.3) presented in Fig. 4.4(c) can be verified. We provide the numbers for power flow, S_{f} and S_{b}, and the reflection coefficients at M_1 and M_2, $|\Gamma_1|^2$ and $|\Gamma_2|^2$, in the caption of Fig. 4.5, and these produce the corresponding pressure points in Fig. 4.4.

4.5 Analytical Description of Enhanced Cavity Pressure

Equation (2.1) provides a simple, approximate means to develop an analytical pressure expression for the 1D cavity. We assume a backward power flow in the cavity given by

$$S_b = \alpha Q S_i, \tag{4.9}$$

where α is a constant that relates Q to Poynting vector magnitude. Upon neglecting the transmission through Mirror 1 and assuming high Q such that the pressure due to the excitation light on Mirror 1 can be neglected, (2.1) yields

$$P_{\mathrm{M}_1} = -\frac{S_b}{c}\left(1 + |\Gamma_1|^2\right) \tag{4.10}$$

$$= -\frac{\alpha Q S_i}{c}\left(1 + |\Gamma_1|^2\right). \tag{4.11}$$

Similarly, the pressure on M_2 can be written as

$$P_{\mathrm{M}_2} = \frac{\alpha Q S_i}{c}\left(1 + |\Gamma_2|^2\right). \tag{4.12}$$

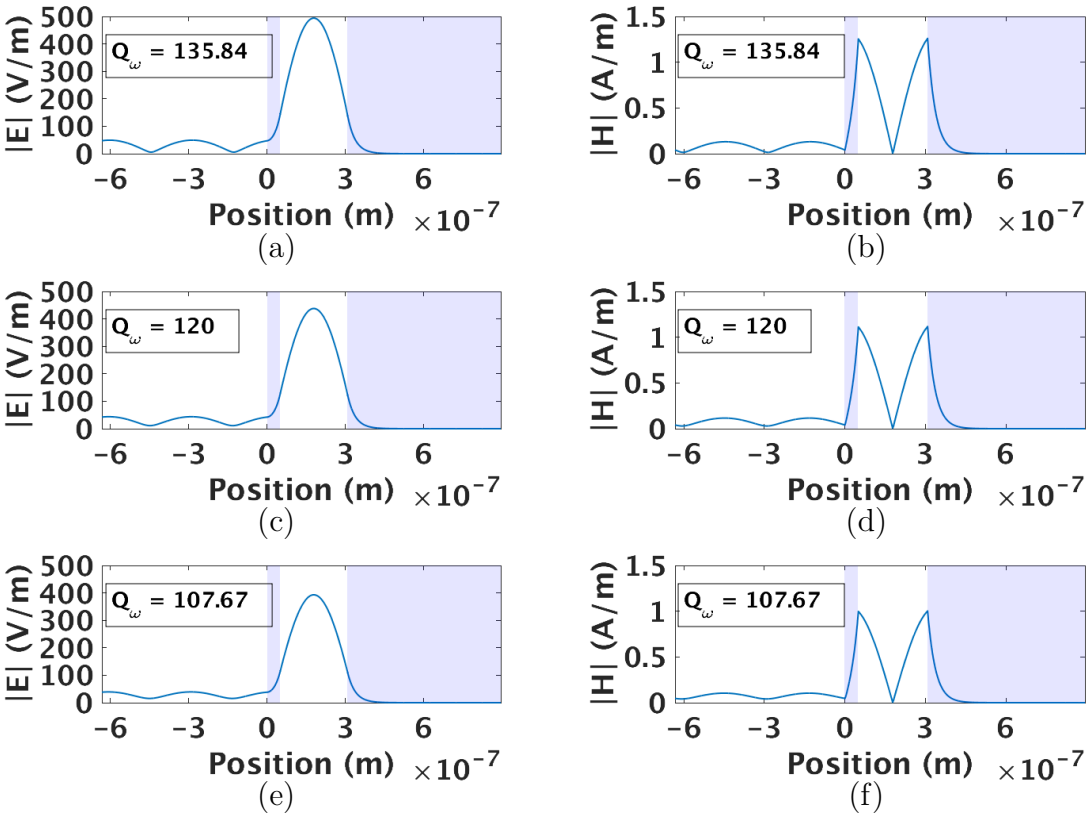

Fig. 4.5. Calculated analytical fields in the asymmetric 1D cavity as a function of propagation distance for the three AFP3 examples with the largest Q ($Q_\omega = 135.84, 120, 107.67$ when $\epsilon''_{M_1} = 0, 0.1, 0.2$, respectively) in Fig. 4.4. (a) Magnitude of the electric field and (b) magnitude of the magnetic field as a function of axial position through the cavity and the mirror regions for $\epsilon''_{M_1} = 0$. The shaded area indicates the positions of M_1 and M_2. (c) Magnitude of the electric field and (d) magnitude of the magnetic field as a function of axial position for $\epsilon''_{M_1} = 0.1$. (e) Magnitude of the electric field and (f) magnitude of the magnetic field as a function of axial position for $\epsilon''_{M_1} = 0.2$. The fields satisfy the boundary conditions and represent the unique solutions for first resonance that is used to produce the corresponding data points in Fig. 4.4. From Fig. 4.2(d), with $S_i = 1$ W/m^2, for $\epsilon''_{M_1} = 0$, $S_f = 81.17$ W/m^2, $S_b = 80.80$ W/m^2 and $|\Gamma_1|^2 = 0.9610$ ($Q_\omega = 135.84$); for $\epsilon''_{M_1} = 0.1$, $S_f = 63.8$ W/m^2, $S_b = 63.51$ W/m^2 and $|\Gamma_1|^2 = 0.9557$ ($Q_\omega = 120$); for $\epsilon''_{M_1} = 0.2$, $S_f = 51.41$ W/m^2, $S_b = 51.17$ W/m^2 and $|\Gamma_1|^2 = 0.9504$ ($Q_\omega = 107.67$). In all the cases, $|\Gamma_2|^2 = 0.9955$. The corresponding data points in Fig. 4.4(c) based on (2.1) are obtained with these numbers (at least to the approximation neglecting the pressure of the excitation light and transmission through M_1).

Summing (4.11) and (4.12), we have

$$P_{\mathrm{M_1+M_2}} = \frac{\alpha Q S_i}{c}\left[|\Gamma_2|^2 - |\Gamma_1|^2\right]. \tag{4.13}$$

Consider the case of an asymmetric cavity where $|\Gamma_2| = 1$, so (4.13) becomes

$$P_{\mathrm{M_1+M_2}} = \frac{S_i}{c}\alpha Q\left[1 - |\Gamma_1|^2\right]. \tag{4.14}$$

We note that $\Gamma_1 = f(Q)$ is smooth but nonlinear. This allows a local, linear approximation for a range of Q and hence a simple means to incorporate this dependence into (4.14). Referring to (4.14), we set $\gamma = 1 - |\Gamma_1|^2$ and use the local linear relationship

$$Q = a\gamma + b. \tag{4.15}$$

Substituting $1 - |\Gamma_1|^2 = \gamma = (Q - b)/a$ into (4.14), we have the quadratic equation in Q as

$$P_{\mathrm{M_1+M_2}} = \frac{\alpha S_i Q}{ac}\left[Q - b\right]. \tag{4.16}$$

Using this simple, analytical picture, we can gain insight into the enhanced pressure regime in Fig. 4.3(a) and where the maximum $P_{\mathrm{M_1+M_2}}$ occurs. Equation (4.16) assumes $|\Gamma_2|^2 = 1$ and AFP3 in Fig. 4.2(a) uses $|\Gamma_2|^2 = 0.9955 \approx 1$. Therefore, we can use Fig. 4.2(a) to find Q and hence α in (4.12). This procedure yields $\alpha = 0.2027$. Because we calculate Q_ω and (4.16) is a function of Q, we use the asymmetric cavity data point with $t = 50$ nm which shows the largest pressure enhancement in Fig. 4.3(a) to relate Q_ω to Q by $Q = \beta Q_\omega$. Note that this point is also the one in AFP3 with the second largest Q (blue star in Fig.4.2(a)). Therefore, with use of Fig. 4.2(a), we find $\beta = 2.6073$. We then write

$$Q_\omega = \frac{1}{\beta}\left(a\gamma + b\right) \tag{4.17}$$

$$= a_n\gamma + b_n, \tag{4.18}$$

where $a_n = a/\beta$ and $b_n = b/\beta$.

Figure 4.3(b) shows calculated points ($t = 40, 50, 70$ and 80 nm) for Q_ω as a function of $\gamma = 1 - |\Gamma_1|^2$. The blue line in Fig. 4.3(b) is the least mean-square error

fit to the points and is selected as a line to determine $Q_\omega = a_n\gamma + b_n$. We thus obtained the parameters $a_n < 0$ and $b_n > 0$ in (4.16), and $a_n = -4.5350 \times 10^3$ and $b_n = 407.3813$. Use of (4.16) with either Q or Q_ω, related by $Q = \beta Q_\omega$, can thus be used to find the local approximation to $P_{\mathrm{M}_1+\mathrm{M}_2}$ and this is the (red) parabola plotted in Fig. 4.3(a). The local maximum of the enhancement occurs when Q_ω is around 200. Notice that this simple, locally linear description nicely captures the essence of the pressure enhancement. A series of such local solutions will provide the set of perturbational solutions.

4.6 Pressure with a Slot Array in a Metal Film

To obtain the fields and the corresponding radiation pressure in the nanostructured slot cavity in a metal film, shown in Fig. 4.1(c), we use a frequency domain finite element method (FEM) to obtain the numerical field solutions [25]. Port boundaries are used in this 2-D model to extract S_{11} and placed $5\lambda_0$ above and below the structure in Fig. 4.1(d). To avoid singularities in the numerical simulations, the corners of each slot are rounded with radius of 1 nm. The maximum mesh element size in the scattering material is $\lambda_0/200$, sufficient to ensure the accuracy of the force density solutions. The slot depth, D, and width, Σ, are variables and the period is set to $\Lambda = 400$ nm and thickness to $T = 200$ nm. With a period of $\Lambda = 400$ nm, only the zeroth-order (normal) scattered plane wave propagates. We fix Σ and vary D to determine the resonant depth from the minimum of $|S_{11}|$.

The results for the slot resonant D as a function of Σ, labeled by the (red) diamonds, are shown on the right axes in Figs. 4.6(a) and (b). A reducing slot width results in a decreasing slot depth for the first resonance. We apply (4.8) to estimate Q_ω for the slot cavity, and the results are shown in Fig. 4.6(a) by the (black) triangles in conjunction with the left axis. Note that Q_ω increases with decreasing Σ, which can be understood by the cavity reflection coefficient at the top of the slot increasing as Σ is reduced, thereby increasing the lifetime of the guided-wave resonance in the

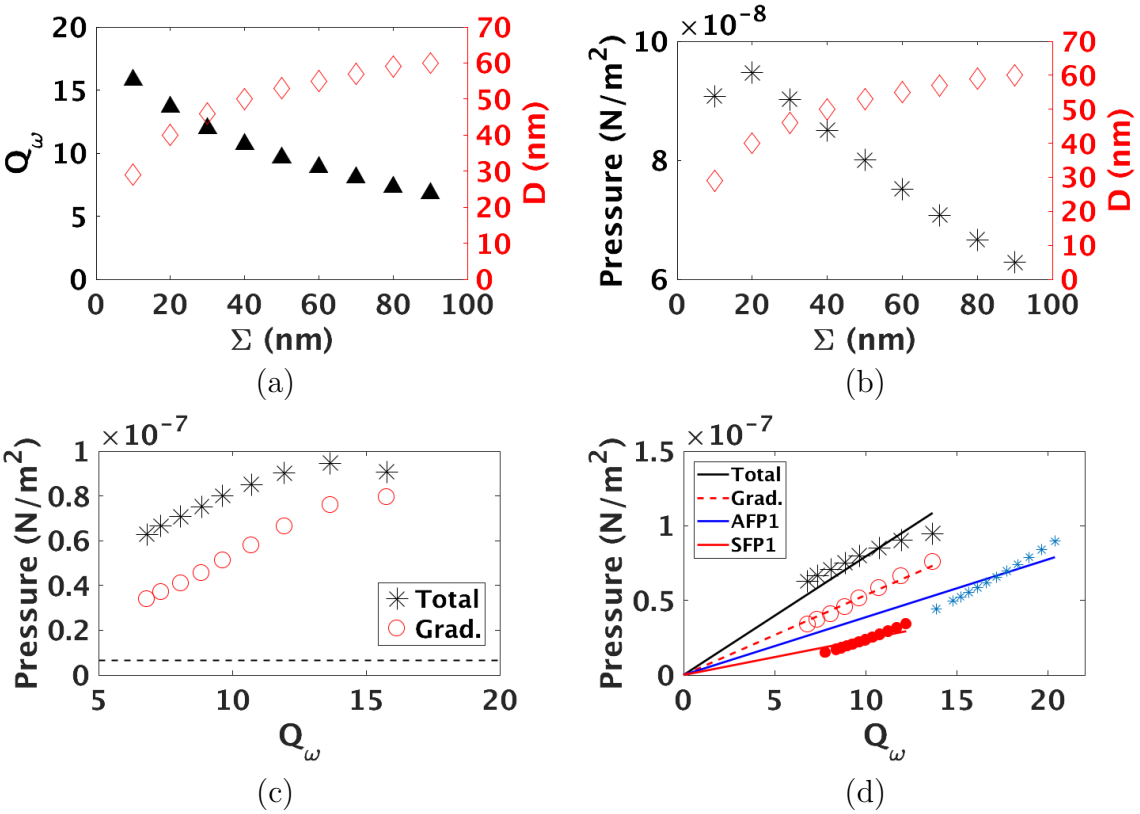

Fig. 4.6. Simulation results for the nanostructured slot cavity array in Au, and with reference to Fig. 4.1(d): $\Lambda = 400$ nm, $T = 200$ nm, Σ is fixed, and D is varied to determine the resonant depth D from the minimum of $|S_{11}|$. (a) Q_ω (triangles) and resonant slot depth, D (diamonds), as a function of slot width, Σ. (b) Radiation pressure (asterisks) along with the resonant D (diamonds) as a function of Σ. In general, smaller Σ results in higher Q_ω and larger pressure, consistent with the asymmetric 1D Fabry-Perot cavity results of Fig. 4.2(d), AFP3. (c) Radiation pressure as a function of Q_ω, decomposed into total and gradient ($\langle \mathbf{f_G} \rangle$) contributions. The dashed line shows the maximum pressure on a perfect mirror. The nanostructured slot cavity supports a pressure enhancement more than an order of magnitude higher than a perfect mirror. (d) Radiation pressure as a function of Q_ω for the lower Q 1D cavities, from Fig. 4.2, in comparison with the slot pressures from (c). The black line and red dashed line are the linear fits to the total pressure and $\langle \mathbf{f_G} \rangle$, respectively from the first 8 points in (c). The blue and red lines are the linear fits to P_{M2} for AFP1 and SFP1, which are low-Q Fabry-Perot cavities in the examples considered. The nanostructured slot cavity is more efficient in delivering radiation pressure enhancement on a target surface than the 1D Fabry-Perot cavity when the cavities have the same Q.

slot and hence Q_L. The numerical field solutions are used in (2.3) to find the force density, and this is integrated over the support of the material within the unit cell and divided by Λ to form the pressure, with the results given by the (black) asterisks for each value of Σ in Fig. 4.6(b), as indicated on the left axis. The general trends in Figs. 4.6(a) and (b) are that both Q_ω and pressure decrease with increasing slot width (at resonance). The pressure results for the slot cavities in Fig. 4.6(b) are consistent with the asymmetric 1D Fabry-Perot cavity results of Fig. 4.2(c) for AFP3, where the pressure increases with Q_ω. The anomalous pressure result for the smallest Σ in Fig. 4.6(b) occurs because of the small slot size and the reduced interaction between the field and the material. Figure 4.6(c) shows the pressure as a function of Q_ω for the slot structures. Unlike the 1D Fabry-Perot cavities, the gradient force term, $\langle \mathbf{f}_\mathrm{G} \rangle$, contributes. We separate the contribution of $\langle \mathbf{f}_\mathrm{G} \rangle$ from the total pressure (black asterisks), and the results are plotted as the red circles in Fig. 4.6(c). In general, the pressure is proportional to Q_ω and the relationship is linear for lower Q_ω. Higher Q_ω supports a higher pressure contribution from $\langle \mathbf{f}_\mathrm{G} \rangle$, associated with the reducing slot width, although the total pressure reduces slightly at the highest Q_ω. The dashed line is again the maximum pressure on a perfect mirror, from Fig. 4.2(c). Compared to the net pressure for the AFP3 1D cavity case in Fig. 4.2(d), the slot cavity can provide a pressure enhancement more than an order of magnitude higher than a perfect mirror with a relatively low-Q cavity. The gradient of the total pressure in Fig. 4.6(c), dP/dQ_ω, describes the efficacy of the cavity in enhancing the pressure (per unit Q or stored energy). In Fig. 4.6(d), we plot the linear fits passing through the origin for the total pressure and the pressure contributed by $\langle \mathbf{f}_\mathrm{G} \rangle$ as black and red dashed lines, respectively, using the first 8 points (linear region) in Fig. 4.6(c). Linear fits to the pressure as a function of Q_ω for SFP1 and AFP1, which involve similar (low) Q_ω to the slot cavity, are plotted for comparison as the red and blue lines, respectively, in Fig. 4.6(d). The nanostructured slot cavity can provide larger pressure enhancement on the target surface than that (on M_2) for the 1D Fabry-Perot cavities we considered when the cavities have the same Q. This is mainly due to the contribution of the

gradient force, $\langle \mathbf{f}_{\mathrm{G}} \rangle$. Consequently, for an incident wave with time-averaged intensity S, the nanostructured slot cavity can utilize the energy stored in the cavity more efficiently in creating optomechanical pressure by drawing on both $\langle \mathbf{f}_{\mathrm{R}} \rangle$ and $\langle \mathbf{f}_{\mathrm{G}} \rangle$.

4.7 Conclusion

We have shown that an asymmetric optical cavity can lead to a total pressure as the sum of that on each mirror that exceeds the pressure on a perfect mirror. This net pressure is substantial by virtue of the asymmetry and can be controlled by cavity Q. The enhanced pressure for the nanostructured metal film results from both terms in (2.3), where the cavity mode resonance influences the fields in the metal and hence the force density and pressure. Generally, increasing the cavity Q can produce higher pressure in the metal film slot resonators. The kinetic force density in (2.3) is derived using conservation of momentum (see [23], for example). Consequently, there is a rigorous basis for the pressure results shown.

The 1D cavity provides a simple vehicle to understand enhanced optical pressure, defined as the sum of the pressure on both mirrors in a Fabry-Perot cavity. With planar mirror and the neglection of transmission, the simple pressure description from Maxwell in (2.1) holds and provides a useful comparison and the basis for a mathematical picture of pressure enhancement. We have provided a rigorous physical and mathematical pressure development and results. However, there is a consistent qualitative picture. Conservation of energy has been demonstrated in our results (Fig. 4.2(d)). The large cavity fields and power flow imply an accumulation of photons and a larger number of photons per unit time striking the interior walls of the cavity than is the case for the external mirror surface through which excitation occurred. The cavity could have been populated with photons by some other means, such as an internal antenna. Regardless, with appreciable cavity field enhancement, the pressures from inside dominates. With the introduction of asymmetry in the cavity mirrors, the pressure on one mirror can exceed the other by an amount that is

greater than the equivalent excitation light applied to a perfect, planar mirror. As we have shown, this can occur with satisfaction of energy and momentum conservation.

A surface plasmon is excited in the slot cavity, associated with the lowest-order MIM mode that propagates for arbitrarily small slot width, allowing for very small cavities. However, other cavity modes using other materials, including dielectrics, are expected to also provide pressure enhancement. This is illustrated in the 1D cavity results we showed, where a surface plasmon was not excited in the metal-like mirrors, and these could have been replaced with dielectric counterparts with similar results.

There are convenient fabrication methods to form nanocavity arrays in metal, for example, direct nanoimprinting [45]. With use of optimized, aperiodic structures, more control and higher pressure should be possible [46], and regulation of the pressure as a function of wavelength should be possible. The explanation for enhancement we have provided allows design guidelines for applications that will benefit from enhanced and controllable optical forces with structured material. For example, beads that are used in optical tweezers could be structured [47]. Also, the efficacy of vehicle propulsion using structured materials should improve. More generally, we suggest that there are new opportunities related to the interaction of waves with structured, resonant materials and the generation of a mechanical response.

4.8 Contribution

Li-Fan was responsible for the numerical simulation and assisted in analytical calculation and analysis of results.

5. ENHANCED PUSHING/PULLING FORCE FROM PLASMONIC SURFACE WAVE

The interaction between light and material is of fundamental importance. Stemming from Maxwell's picture, the maximum time-averaged radiation pressure is achieved with a perfect mirror. However, recent experimental evidence has confirmed that this pressure can be exceeded by a substantial factor by structuring the surface of a metal and exciting plasmon mode resonances. While a negative force can be imparted on a small particle by control of an optical beam, entire structures are generally thought to be only pushed by incident light. Recently, a statistical simulation study of aperiodic dielectric and metal elements provided example structures that could be pulled as well as pushed, with evidence of a relationship to the character of resonances. We propose a simple transverse resonant system that can either be pushed or pulled, depending on dominant fields being established on the front or back, respectively. In this work, pulling is achieved by exciting a plasmonic wave resonance on the back side of Au/SiN membrane, excited by a coupling slot. We demonstrate that both the pushing and pulling pressures can exceed that on a perfect mirror and can be controlled based on wavelength with light incident from a single direction. Being able to push and pull structures will be of value in actuation and propulsion applications.

5.1 Introduction

Maxwell's picture predicts the maximum pressure on a perfect mirror. However, we discovered that the optical pressure on a structured metal surface can be substantially enhanced greater than that on a planar surface [24], and demonstrated it with the optomechanic deflection experiment [15]. We interpreted this phenomenon with momentum conservation by introducing asymmetric cavity picture with appropriate

quality factor [16]. While the 1D asymmetric cavity provides insight into pushing pressure enhancement, we characterized that the field resonance on the material surface will results in enhanced not only pushing but also pulling pressure with aperiodic structure [48]. The work gives concept of enhanced pulling pressure, but will still require a compact physical picture with simple system to illustrate the relation between enhanced pulling pressure and resonant field on the other side of the structure. Here we present the understanding of promoting enhanced pushing and pulling pressure by exciting resonant confined field on the same side or the opposite side (to the incident light) of the membrane. The pulling pressure under this concept can be easily captured as a pushing pressure pushing against the direction of the incident light.

We investigate this by looking into plasmonic surface wave on a nano-slotted Au membrane. The resonant transverse surface wave will be excited through metal-insulator-metal (MIM) cavity mode. Allowing resonant surface wave on either side of the membrane, enhanced pushing or pulling pressure is promoted. Applying the finite element method [25] for the field solution and the force density equation (2.3), we obtain interesting examples displaying enhanced pushing and pulling pressure. Further more we present that the pushing and pulling opto-mechanics can be controlled by different wavelength on the same designed structure. With the understanding of the relation between enhanced pushing/pulling pressure and the plasmonic surface wave, it will guide us to the design of structured metallic and dielectric materials where increasing in pushing and pulling pressure over that on a perfect mirror is possible. This will provide useful in applications, especially those where a restoring force may otherwise be unavailable.

5.2 Single Au Layer

We consider a transversely periodic geometry of slotted Au membrane as shown in Fig. 5.1(a), where Λ is the periodicity, W is the slot width, and T is the Au thickness. In the simulation setup the periodic boundary is placed at the left and right forming

a periodic structure. The perfectly matched layer (PML) is placed at the top and bottom. A 633 nm plane wave with **H** out of the plane is illuminating (the red arrows) from the top. The intensity of the light is equivalent to 1 mW over 1 μm radius circle. The corners are rounded with a 2 nm quarter circle to avoid numerical sharp corner effect. The time-averaged y-directed force density in the materials can be found by (2.3), and the collective y-directed pressure, assuming z-invariant structure, is calculated by integrating the force density over the unit cell area (x - y plane) and divided by the unit cell width (Λ). This allows obtaining the vertical pressure on the periodic structure. The basic concept of this structure is that the incident light will be coupled into the slotted structure and then excites the transverse waveguide mode(s) that facilitates the control of the net force. Using relatively simple pictures, such as surface wave and MIM mode excitation [49–52], we can establish the underlying principles.

We can estimated the transverse wavelength of the plasmonic surface wave on the top and bottom of Au at the metal-dielectric interface in Fig. 5.1(a) (here the dielectric is air) from

$$\beta = k_0 \sqrt{\frac{\epsilon_1 \epsilon_2}{\epsilon_1 + \epsilon_2}}, \tag{5.1}$$

where β is the propagation wave vector of the surface wave, k_0 is the incident wave vector in free space, ϵ_1 is the dielectric constant of the dielectric material, and ϵ_2 is the dielectric constant of the metal. The dielectric constant for Au assumed is -11.8 + i1.23 [26] for 633 nm wavelength. From (5.1) the estimated propagation wavelength of the surface wave on air-metal interface is around 620 nm.

We then fix Λ at 620 nm with 60 nm W, then vary T from 100 nm to 500 nm. The calculated pressure is shown in Fig 5.1(b). In the figure, the dashed red line indicates the pressure on a perfect mirror with same intensity. The dashed black line is the zero pressure. We indicate the region above the dashed black line to be pulling pressure region and the under the pushing pressure region because the plane wave is illuminating from the top in the $-$y-direction. Figure 5.1(c) plots the power density on the bottom side of the Au membrane, i.e. the power density through the

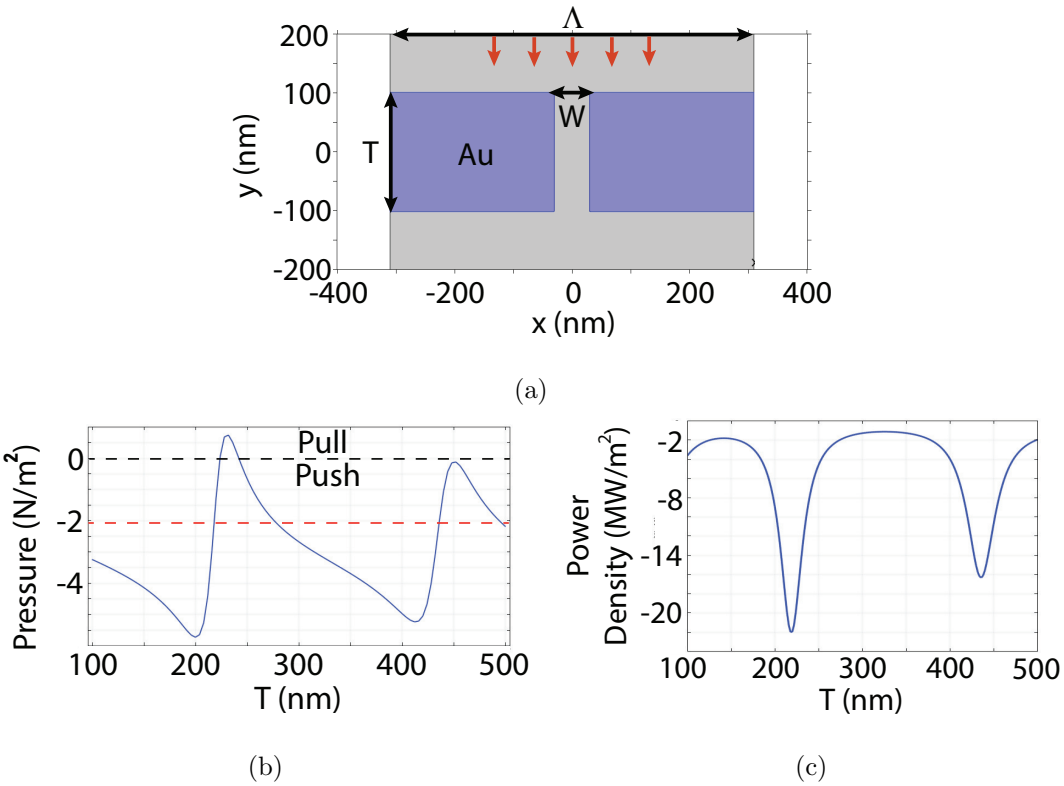

Fig. 5.1. Simulation of a periodic nanoslotted Au ($\epsilon = -11.8 + i1.23$) membrane illuminated by light. (a) Simulation setup with parameters: period Λ, slot width W fixed at 60 nm, and Au thickness T. The 633 nm plane wave with **H** out of plane is illuminated from the top, and the intensity is equivalent to 1 mW over 1μm radius circle. (b) Calculated time-averaged y-directed pressure with $\Lambda = 620$ nm, and T from 100 nm to 500 nm. The dashed red line indicates the pressure on a perfect mirror with same intensity, and the dashed black line is the zero pressure. We indicate the region above the dashed black line to be the pulling pressure region and under the pushing pressure region because the plane wave is illuminating from the top in $-$y-direction. (c) Calculated power density on the bottom side of the Au membrane pointing in $-$y-direction, with respect to T. Note that pulling pressure in (b) is promoted when the power density on the bottom side of Au is increased. The length between the two peaks in (b) and (c) indicates the MIM mode cavity resonance.

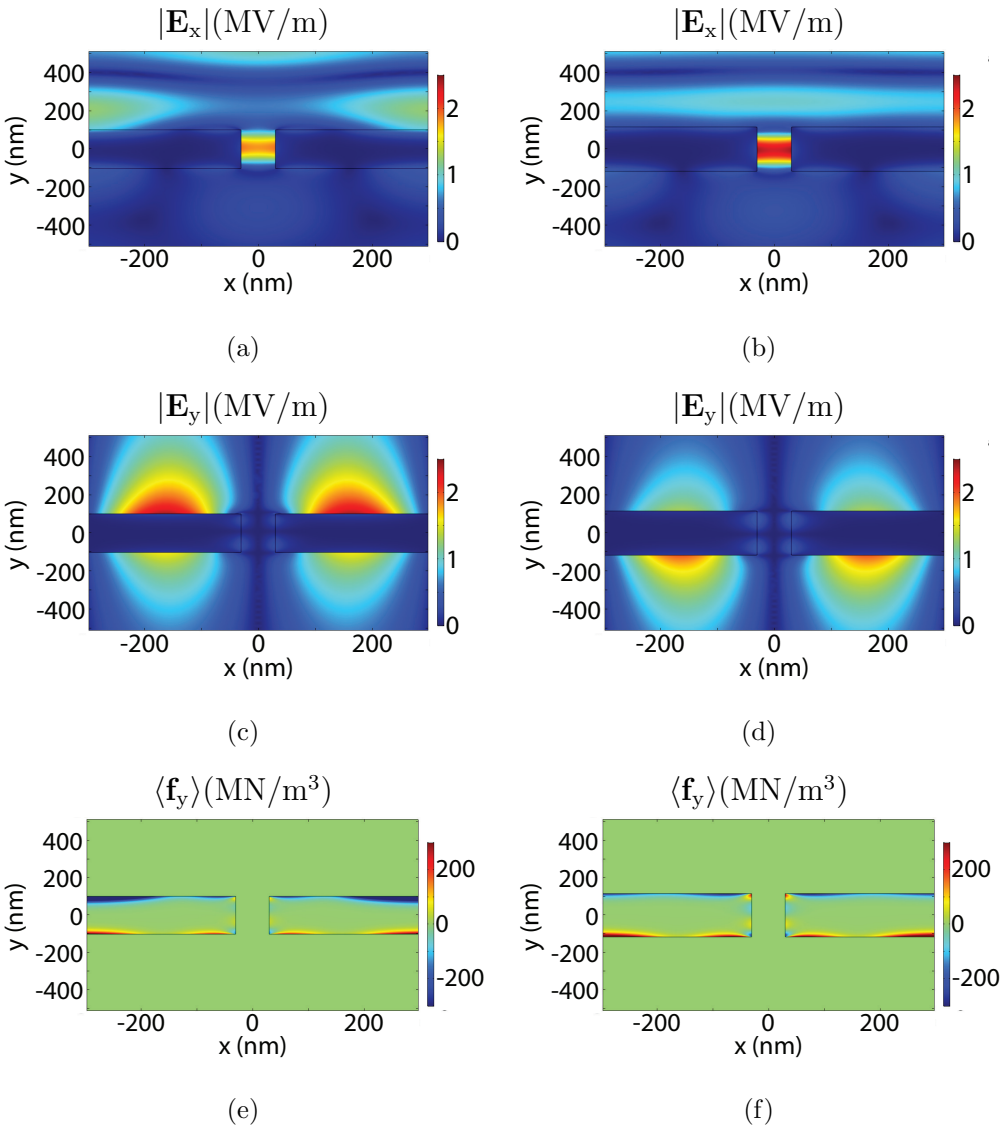

(a) (b) (c) (d) (e) (f)

Fig. 5.2. Simulation results of the largest pushing and pulling pressure in Fig. 5.1(b) around T = 220 nm. The largest pushing pressure, -5.77 N/m^2, occurs at T = 203 nm. Increasing T to 232 nm will shift the pushing pressure to the pulling pressure, 0.77 N/m^2. Calculated field and force density distribution of the pushing and pulling cases are plotted. (a), (c), and (e) show the x-directed electric field magnitude, y-directed electric field magnitude, and y-directed force density, respectively, for T = 203 nm, and (b), (d), and (f) the x-directed electric field magnitude, y-directed electric field magnitude, and y-directed force density, respectively, for T = 232 nm. From x- and y-directed electric field distribution, we can see that the resonant MIM wave in the slot cavity promotes the resonant surface wave on the top and bottom of Au, and as a result develops large force density on both surface However we can see that the force density from the surface wave on the top and bottom competes each other and therefore reduces the magnitude of pushing and pulling pressure.

Au slot, with respect to T, pointing to the −y-direction. Comparing Fig. 5.1(b) and (c) we can see that the pulling pressure is promoted when the power density on the bottom side of Au membrane is increase. This can be understood as the field forming the surface wave on the bottom side of the Au which produces pushing force density against the direction of the incident light to the Au, This will be demonstrated in Fig. 5.2. This phenomena can also be interpreted from the momentum exchange view that the pulling force on the bottom of the membrane is induced by the photon momentum leaving the surface of Au. Figure 5.1(b) and (c) show a periodic variation of calculated pressure and peak power density around 220 nm. This can be suggested as the MIM mode resonant wavelength inside the cavity. Also larger T suggest larger loss, therefore from 5.1(b) and (c) the promoted pulling pressure magnitude as well as the power density on the bottom side of the Au decrease when T increase.

Figure 5.1(b) shows that the largest pushing pressure occurs at T = 203 nm. The pushing pressure, -5.77 N/m^2, is about 3 times greater than that on the perfect mirror. Increasing T to 232 nm will shift the pushing pressure to the pulling pressure, 0.77 N/m^2. We investigate the field solution and calculated the force density distribution of the two corresponding Au thickness. Figure 5.2(a), (c), and (e) show the x-directed electric field magnitude, y-directed electric field magnitude, and y-directed force density, respectively, for T = 203 nm, and (b), (d), and (f) the x-directed electric field magnitude, y-directed electric field magnitude, and y-directed force density, respectively, for T = 232 nm. From x- and y-directed electric field distribution, we can see that the surface wave on the top and bottom of the Au are developed with resonant MIM mode in the slot as shown Fig. 5.2(a) to (d). We here suggest that the surface wave on the top and bottom of Au are promoted by the MIM wave resonance in the slot cavity. That is without the resonant MIM mode in the slot, there will be no enhanced surface wave. This will be demonstrated in Fig. 5.3. When T = 203 nm, less surface wave is developed on the bottom of Au, shown in Fig. 5.2(c), and result in collective large pushing pressure shown in Fig. 5.2(e). On the other hand, when T is increased to 232 nm, the surface wave at the bottom is stronger

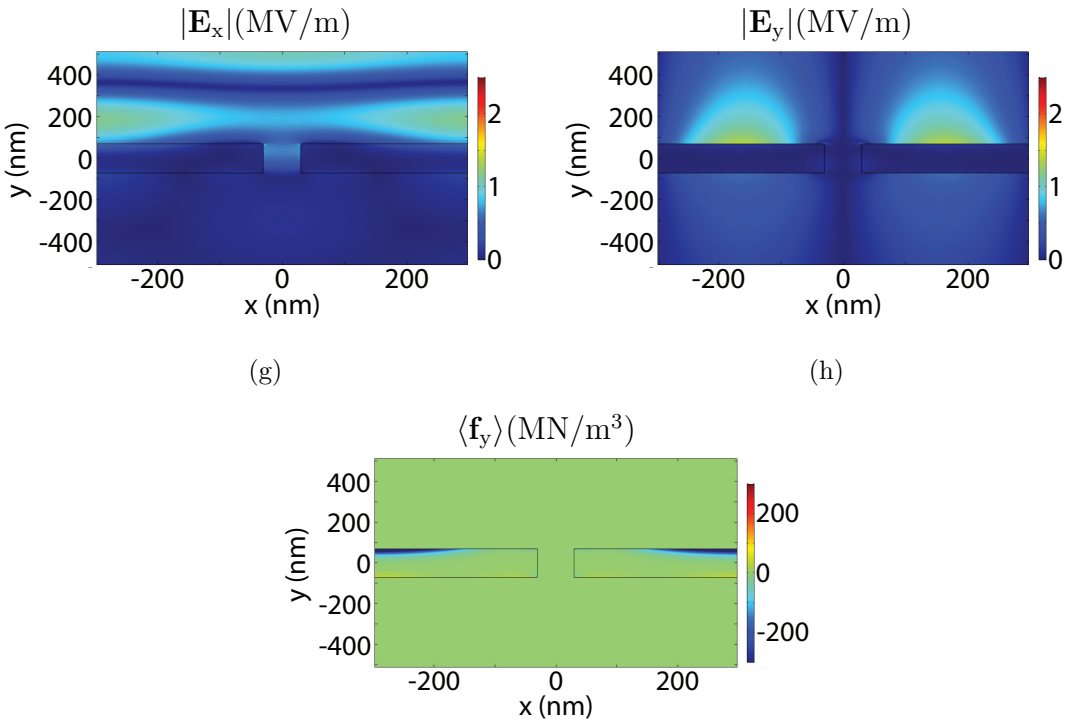

Fig. 5.3. Simulation result of the field and force density when T = 140 nm away from the cavity MIM resonance, where the power density through the slot is small in 5.1(c). (a) to (c) show the x-directed electric field magnitude, y-directed electric field magnitude, and y-directed force density, respectively. From (a) the MIM mode is not resonant in the cavity, resulting in weak top and bottom surface wave in (b). This suggests that the resonant MIM mode in the cavity promotes the top and bottom surface wave. However in (b) there is still larger surface wave on the top than on the bottom resulting in more pushing force density on the top of Au, shown in (c). There is a collective pushing pressure of -3.8 N/m^2.

than that on the top, shown in Fig. 5.2(d). However the field magnitude difference between the top and the bottom surface wave in the pulling pressure case is much less than that in the pushing pressure case, resulting in collective small pulling pressure on Au (Fig. 5.2(f)). From the two cases, especially the enhanced pushing pressure when T = 203 nm, the plasmonic surface wave can evidently enhanced the pressure magnitude greater than that on a perfect mirror. However, we also learn that the co-existed surface waves on the top and the bottom of Au will compete each other and therefore limits the enhancement of the collective pressure.

Figure 5.3(a) to (c) show the x-directed electric field magnitude, y-directed electric field magnitude, and y-directed force density, respectively, for T = 140 nm, which is away from the MIM resonant cavity length. The MIM mode is not resonant due to the slot cavity condition shown in Fig. 5.3(a). The top surface wave becomes weak and the bottom surface wave disappears. This verifies our suggestion that the resonance of the MIM mode promotes the top and bottom surface wave. However from Fig. 5.3(b) and (c) there are still some surface wave and the force density on the top, resulting in collective pushing pressure, -3.8 N/m^2, which is still slightly greater than that on the perfect mirror.

5.3 Double Layer with SiN on Top of Au

Single Au layer condition provides direction on designing enhanced pushing or pulling pressure on a thin membrane by manipulating the top and bottom surface wave. If either top or bottom surface wave is annihilated, optical pressure can be greatly enhanced. One approach to eliminate one side of the surface wave is to develop different surface wave propagation wavelength between the top and bottom of Au and modify the periodicity to match one of the surface wave wavelength. This can be achieved by adding dielectric layer to the top or bottom of Au. Figure 5.4(a) shows this simulation setup for enhanced pushing pressure. We add a 50 nm SiN layer, refractive index of 2 at 633 nm wavelength, to the top of Au. The 50 nm

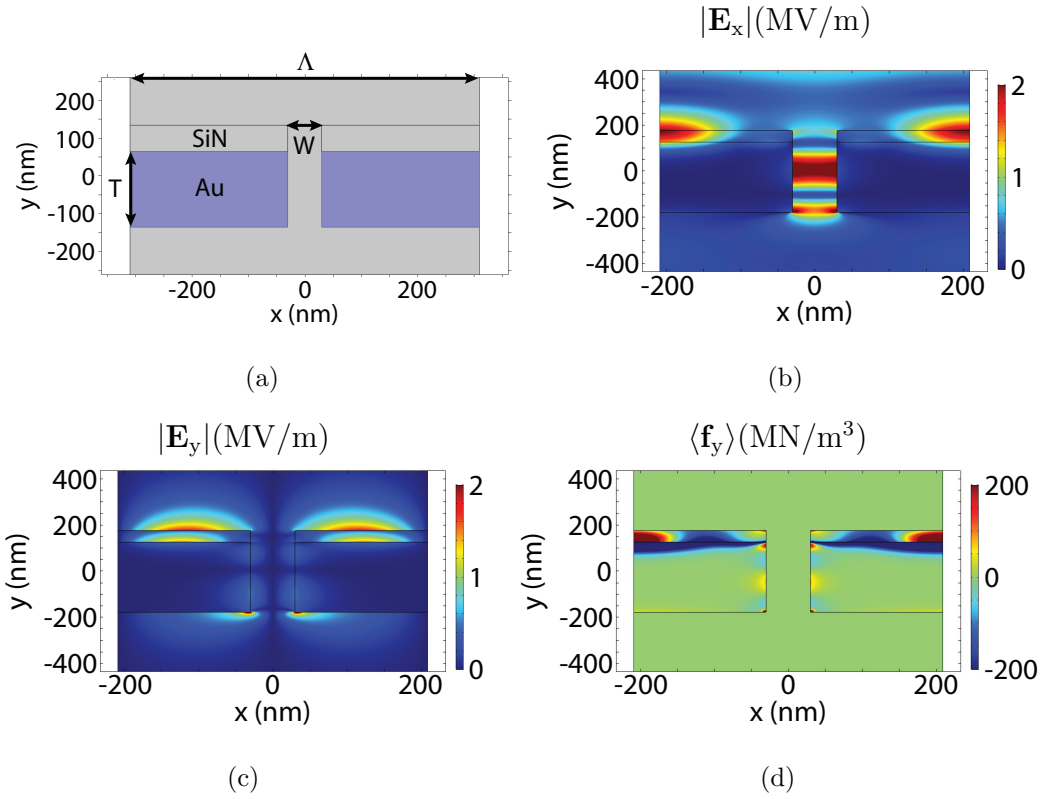

Fig. 5.4. Simulation results of enhanced pushing pressure -20.3 N/m^2 by adding 50-nm SiN layer (n = 2) to the top of Au. (a) Simulation setup with parameters: Λ = 418 nm, W = 60 nm, T = 304 nm. The incident wave is illuminated from the top with intensity equivalent to 1 mW over 1 μm radius circle. (b) x-directed electric field magnitude (c) y-directed electric field magnitude (d) y-directed time-averaged force density From (b) the MIM mode is resonant inside the cavity which promotes the surface wave on the top of Au in (c). Λ is varied from that in Fig. 5.1 such that the bottom surface wave is not developed via resonance. Due to the absence of bottom force density shown in (d), the collective pushing pressure is enhanced greater than that without SiN layer. We can also see that the field is coupled into force density in the SiN layer which produces pressure. The pressure in SiN layer is -0.8 N/m^2 and in Au is -19.5 N/m^2, so that the field in Au dominates the enhancement of pressure.

thickness is selected due to the commerically available product from Norcada. The modified wavelength of the surface wave between Au and SiN can be roughly estimated by (5.1) and will depend on the thickness of SiN layer. The dependence can be understood from that the effective refractive index on the SiN side is characterized by the proportion of the evanescent field inside the SiN. That is the thicker the SiN layer the more the effective refractive index will approach 2 and the shorter the propagating wavelength of the surface wave will be.

By adding SiN layer on the top of Au, we find greatly enhanced pushing pressure -20.3 N/m^2 when $\Lambda = 418$ nm and T = 304 nm with W fixed at 60 nm. Figure 5.4(b), (c), and (d) show the x-directed electric field magnitude, y-directed electric field magnitude, and y-directed force density distribution, respectively, for the enhanced pushing pressure. Figure 5.4(b) and (c) show that the surface wave on the top is excited by the resonant MIM mode in the cavity. Because Λ is varied away from 620 nm, the single Au layer case, the bottom surface wave is not developed due to the non-resonant condition. The excited surface wave on the top of the membrane develops the pushing force density. Without the competition of the bottom pulling force density, the pushing pressure magnitude is greatly enhanced than that on a single Au layer membrane. From Fig. 5.4(c) and (d) field is coupled to force density inside the SiN layer as well. We calculate the pressure separately in SiN and Au and and obtain -0.8 n/m^2 of pushing pressure in SiN and -19.5 n/m^2 of pushing pressure in Au, respectively. This indicates that the pressure produced in Au dominates the pressure enhancement.

5.4 Double Layer with SiN on the Bottom of Au

We have shown that the enhanced pushing pressure by adding SiN layer to the top of Au. We now explore the enhanced pulling pressure by adding a 50 nm SiN layer to the bottom of Au. Figure 5.5(a) shows the simulation setup with SiN layer added to the bottom of Au. When $\Lambda = 420$ nm and T = 320 nm with W fixed at

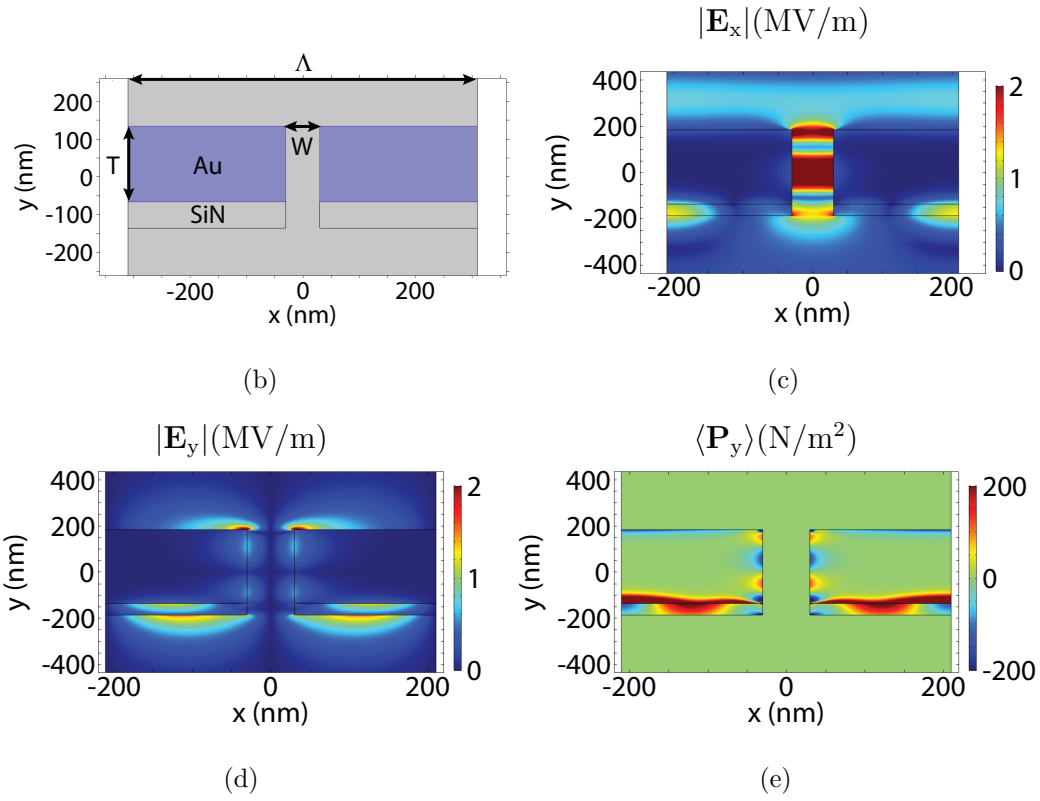

Fig. 5.5. Simulation results of enhanced pushing pressure 10.12 N/m^2 by adding 50-nm SiN layer (n = 2) to the bottom of Au. (a) Simulation setup with parameters: Λ = 420 nm, W = 60 nm, T = 320 nm. The incident wave is illuminated from the top with intensity equivelant to 1 mW over 1 μm radius circle. (b) x-directed electric field magnitude (c) y-directed electric field magnitude (d) y-directed time-averaged force density From (b) the MIM mode is resonant inside the cavity which promotes the surface wave on the bottom of Au in (c). Λ is adjusted to match the resonant wavelength of the bottom surface wave. As a result with the absence of top surface wave as well as the force density on the top of Au, shown in (d), we have enhanced pulling pressure. The calculated pressure in SiN layer is 2.04 N/m^2 and in Au is 8.08 N/m^2.

60 nm, and we find enhanced pulling pressure 10.12 N/m^2. Figure 5.4(b), (c), and (d) show the x-directed electric field magnitude, y-directed electric field magnitude, and y-directed force density distribution, respectively, for the enhanced pulling pressure. In this case, the geometry is similar to the enhanced pushing pressure structure but with SiN layer added to the bottom. T is adjusted to develop MIM mode resonance in the slot cavity shown in Fig. 5.4(b). Then the bottom surface wave is promoted as shown in Fig. 5.4(c). The produced force density on the bottom with the absence of top force density shown in 5.4(d) results in enhanced pulling pressure. Field, same as the enhanced pushing pressure case, is coupled into the force density in the SiN layer. The calculated pulling pressure in SiN is 2.04 N/m^2 and 8.08 N/m^2 in Au, respectively. Compared to the enhanced pushing pressure magnitude when adding SiN to the top of Au, the enhanced pulling pressure magnitude when adding SiN to the bottom of Au is smaller. This can be understood that the bottom surface wave is developed by partially transmitted field through the slot. Therefore with similar structure the magnitude of surface wave as well as the force density on the bottom side of the membrane will be smaller than that on the top side of Au.

5.5 Wavelength Controlled Pushing and Pulling Pressure

We have investigated the physics and guideline of designing for enhanced top and bottom surface wave with enhanced pushing and pulling pressure. We found that the enhanced pressure can be achieved by adding dielectric layer to the top or bottom of Au with the right periodicity. From another view, varying the wavelength of the incident wave achieve the same goal as varying the periodicity for a resonant surface wave. Consequently and methodically, we can design a wavelength-controlled pushing and pulling pressure on the same nano-structure. We now add a dielectric layer to the top and a SiN layer to the bottom of Au. In Fig. 5.6(a), a 10 nm of dielectric layer with different refractive indices (n = 1.5, 2, 2.5) is added to the top of Au and a 40 nm SiN layer is added to the bottom. The top dielectric layer is thinner than the bottom

SiN is because from the previous results we notice that larger pushing pressure is easier to established than the pulling pressure for the same thickness of SiN layer, and thinner top dielectric layer will allow pushing pressure magnitude comparable to the pulling pressure magnitude for practical purpose. We find interesting results when the Au thickness T is 306 nm and the periodicity Λ is 460 nm. Fig. 5.6(b) shows the calculated time-average y-directed pressure by varying the incident wavelength from 400 nm to 800 nm with different refractive index of the top dielectric layer. The refractive index of SiN is 2 at 633 nm, approximated as constant over the wavelength range used. The wavelength depended dielectric constant of Au is applied [26]. In Fig. 5.6(b), the green curve shows the calculated pressure of the original refractive index of 2 of SiN for the top dielectric layer. We can see that around 570 nm incident wavelength the membrane has the the largest pushing pressure about -3 N/m^2 and the largest pulling pressure about 6 N/m^2 around 630 nm incident wavelength. We like to show that, for practical purpose, the magnitude of the largest pushing and pulling pressure and the corresponding wavelength can be adjusted by changing the refractive index of the top dielectric layer. This can also be identified by Eq. (2.3) that the value of refractive index contribute to force density inside the material (from $\mathbf{P}$). In Fig. 5.6(b), the refractive index of the top dielectric layer differs from 1.5 (blue curve), 2 (green curve), and 2.5 (red curve). The corresponding significant changes are presented at the magnitude of the largest pushing and pulling pressure. When the refractive index of the top layer becomes smaller (n = 1.5) even larger pulling pressure (about 8 N/m^2) and smaller pushing pressure (about -2 N/m^2) is realized. On the other hand, the larger refractive index (n = 2.5 the red curve), exhibits a balanced magnitude between pushing and pulling pressure around 4 N/m^2. As a result, if one seeks the pressure control with equal magnitude, the red curve will be a more favorable design. Figure 5.6 presents the schematic with many degrees of freedom to achieve wavelength controlled pushing and pulling pressure on the same structure. For example, the refractive index can be tuned not only on the top but also on the bottom dielectric layer. One can also use the same dielectric material

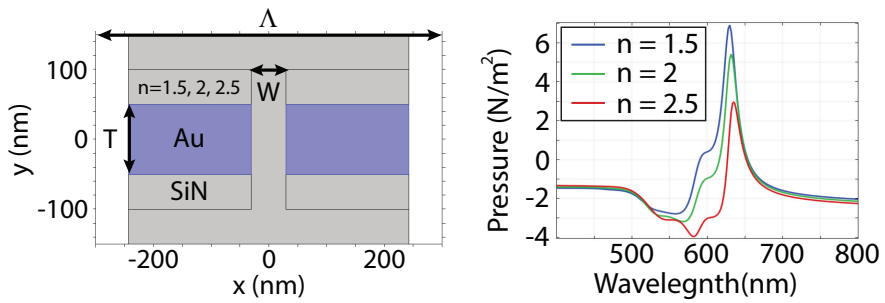

(a) (b)

Fig. 5.6. Calculated wavelength-dependent pressure for a dielectric-clad Au membrane showing pushing (negative pressure) and pulling (positive pressure), depending on wavelength. (a) Geometry with 40 nm SiN ($n = 2$ at 633 nm, approximated as constant over the wavelength range used) on the bottom and 10 nm dielectric with three different refractive indices on top ($n = 1.5, 2, 2.5$). A plane wave is normally incident from the top with an intensity corresponding to 1 mW over 1 μm radius circle. (b) Calculated pressure: $n = 1.5$ (blue curve), $n = 2$ (green curve), and n = 2.5 (red curve) when T = 306 nm, $\Lambda = 460$ nm, and slot width $W = 60$ nm. Note the pushing force (-3 N/m^2) around 570 nm and pulling (6 N/m^2) in the neighborhood of 630 nm when n = 2 for the top dielectric layer.

for the top and bottom layer but with different thickness. As discussed before the thickness of dielectric layer will modify the effective dielectric constant to the surface wave, and from (5.1) the incident wavelength for the resonant top or bottom surface wave will differ due to the different thickness of the dielectric layer.

5.6 Conclusion

Conventionally, when designing for optomechanics to achieve maximum optical force or pressure exerted on the materials, laser propulsion [53] for example, one would follow the principle of (2.1) for design to achieve as high reflectivity as possible. Here we build an understanding of controlling the enhanced magnitude and the pressure direction with the excitation of resonant surface plasmonic waveguide modes in Au (with SiN). The significant physical issue demonstrated in this work is the realization

of a enhanced pushing and pulling pressure greater than that on a perfect mirror by exciting field resonance on either side of the simple structured membrane from a single direction plane wave illumination. The pulling force in this picture can be simply understood as a pushing force on the opposite side of the structure against to the direction of incident wave. This provides the important physics for the guideline of design to achieve pulling force by developing resonant field on the other side the structure, the plasmonic surface wave in our example. We have demonstrated this by binary aperiodic structure using dielectric material and metal [48]. Compared to [48], we propose a simple layer system design to easily achieve pulling pressure. There are others have presented pulling force, for example the tractor beams pulling particles by the control of the incident light [28]. We here present that instead of manipulating the incident light, a simple plane wave incidence on the designed structure which can be easily fabricated can provide enhanced pulling pressure on opto-mechanics. This will open significant opportunities to opto-mechanic applications.

6. STRUCTURED DIELECTRIC OPTOMECHANICS

To circumvent the influence of heating on metals, we take interest in all-dielectric materials where their band gap is beyond the incident wavelength, so no thermal effect will occur. All-dielectric structures offer promise for a range of applications and mitigate heating and thermal deflection. We have learned that regulation of the character of resonances in structured dielectrics can provide for pushing or pulling [48]. However, a simple dielectric film system is of interest for force regulation, including realizing a pulling force.

We discover that from the analytic solution in earlier work, a thin, low dielectric constant film in a higher dielectric constant background can provide a negative force on this film [17]. Then a numerical simulation to demonstrate this will be of interest. On the other hand, from the second term of (2.3), or the gradient term, it reveals that with positive dielectric constant, a pulling force can be established from the evanescent nature of the field. That is, the gradient force can provide the condition for a pulling pressure. One simple way to establish an evanescent field in dielectric material is from internal total reflection, when light is incident from a high dielectric constant region onto a low dielectric constant region above the critical angle. The two strategies are straightforward and easy to fabricate. We will apply silicon (Si) and SiN in our simulation setup, for they are widely employed in the silicon photonics industry.

6.1 Pulling force on dielectric layer in higher dielectric constant background

In the three-region problem discussed in [17], where a slab is embedded in a background material with a specified dielectric constant, the analytic solution of the

optical pressure in the slab suggested that a lower dielectric constant of the slab placed in a higher dielectric constant background can promote pulling pressure with specific slab thickness.

Figure 6.1(a) shows the simulation setup. A dielectric slab with thickness T and refractive index of 2 is sandwiched by two semi-infinite background with refractive index of 4. The light is normally incident from the top with 633 nm free space wavelength. The intensity is equivalent to 1 mW over 1 μm radius circle. Fig. 6.1(b) calculates the y-directed pressure when T varies from 10 nm to 300 nm. Because the light is incident from the top, a positive value indicates a pulling pressure. We observe a periodic variation of pulling pressure with respect to T. We then investigate the electric field and y-directed force density distribution for the largest pressure and the zero pressure cases. Figure 6.1(c) and (e) plot the electric field and force density in the slab, respectively, when T equals to one quarter of a wavelength in the slab. The asymmetric electric field contributes to all pulling force density and therefore promotes the largest pulling pressure. On the other hand, in Fig. 6.1(d) and (f), when T equals to one half of a wavelength in the slab, the symmetric electric field contributes equal amount of the pushing force density to the pulling force density. This results in zero pressure. We can then conclude that the largest pulling pressure occurs on the slab when T = $(2m+1)\frac{\lambda_{n=2}}{4}$, and the zero pressure occurs when T = $(m+1)\frac{\lambda_{n=2}}{2}$, where $m = 0, 1, 2, ...$ and $\lambda_{n=2}$ is the wavelength in the slab (n = 2).

6.2 Pulling Force from Internal Total Reflection

With light incident from a high dielectric constant region onto a low dielectric constant region above the critical angle, an evanescent (decaying) field results in the low dielectric constant region. This can be achieved in a waveguide geometry and by coupling light with a few grating periods formed in the dielectric. Figure 6.2(a) shows the electric field magnitude (with magnetic field out of the page) with oblique incidence from a region with refractive index (n) 4 to a film with refractive index 2

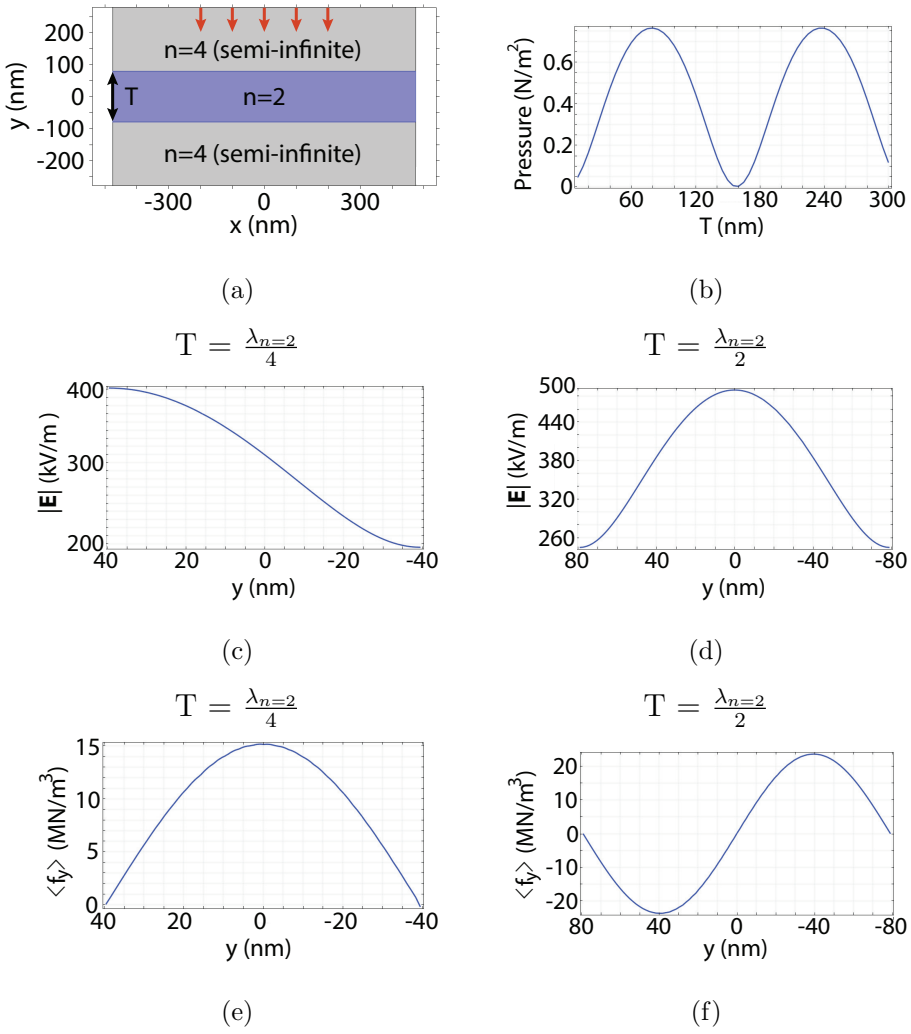

Fig. 6.1. Calculated pressure on a dielectric slab (n = 2) with thickness T sandwiched by two semi-infinite dielectric background (n = 4). A light with 633 nm wavelegnth in free space is normally incident from the top and the intensity is equivalent to 1 mW over 1μm radius circle. (a) Simulation geometry. (b) Calculated pressure on the slab with T varied from 10 nm to 300 nm. (c) Electric field in the slab when T is one quarter of a wavelength in the slab. (d) Electric field in the slab when T is one half of a wavelength in the slab. (e) Y-directed force density in the slab when T is one quarter of a wavelength in the slab. (f) Y-directed force density in the slab when T is one half of a wavelength in the slab. The calculated pulling pressure in (b) presents a periodic variation from 0 N/m^2 to 0.75 N/m^2. The positive value indicates pulling because the light is incident from the top. (c) and (e) show that when T is one quarter of a wavelength in the slab, the asymmetric distribution of the electric field promotes all pulling force density in the slab and therefore produces the largest pulling pressure. On the other hand, (d) and (f) show that when T is one half of a wavelength in the slab, the symmetric distribution of the electric field introduces equal amount of the pushing force density to the pulling force density in the slab and results in zero pulling pressure.

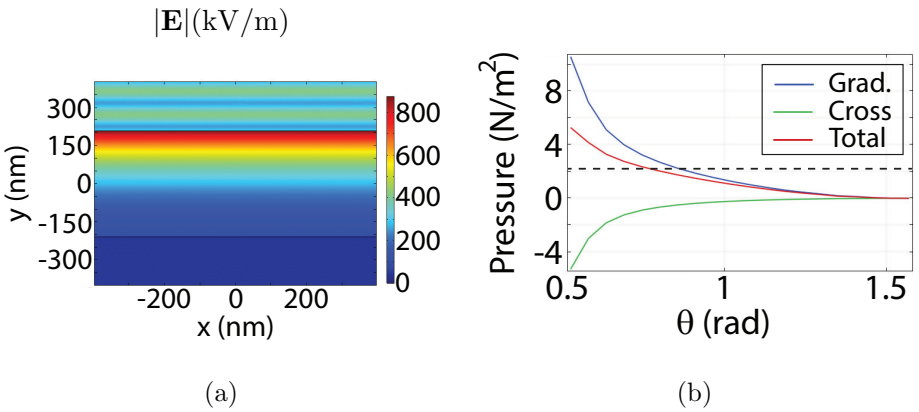

(a) (b)

Fig. 6.2. Simulation of an obliquely-incident plane wave (magnetic field out of the page) from a high refractive index ($n = 4$) material to low refractive index ($n = 2$) film ($-160 \leq y \leq 160$ nm) with a free space wavelength of 633 nm and an intensity corresponding to 1 mW over 1 μm radius circle. (a) Electric field magnitude, showing the evanescent field in the $n = 2$ film. (b) Calculated gradient pressure from the second term in (2.3) (blue curve), Poynting-like pressure from the first, cross term of (2.3) (green curve), and the total pressure (red curve) on the low refractive index material. The black dashed line is corresponding pushing pressure magnitude on a perfect mirror. Note that there is a pulling force for smaller angles (beyond the critical angle) and a pushing force for large angles, allowing the direction of the force to be adjusted with angle.

($-160 \leq y \leq 160$ nm), showing the evanescent field in this region. The resulting pressure determined from (2.3) for the $n = 2$ region is shown in Fig. 6.2(b), with the separation of the terms: cross is the first term in (2.3) (green curve) and gradient is the second (blue curve). Notice from Fig. 6.2(b) that there is a range of incident angles (in the neighborhood of and beyond the critical angle) where the pressure is positive, indicating pulling, and a region where there is a pushing force. We will simulate practical situations that exploit this effect, with the goal of implementation on a SiN membrane.

7. SUMMARY

Maxwell's picture of radiation pressure predicts that the maximum optical pressure could not exceed twice the averaged power density of the incident light divided by the background light speed. This is the case for a perfect, planar mirror, where the force is in the direction of incident light. This conventional view is widely recognized and utilized. We have experimentally demonstrated that with a nanostructured Au film on a SiN membrane, the collective optical pressure can exceed that on a perfect mirror, that is the maximum result predicted by Maxwell's prediction. In the experiment, the enhanced optical pressure is characterized by the membrane deflection and the Einstein-Laub force equation. Applying a 1D cavity model, we attribute the enhancement of the net optical pressure on nanostructured material over that on a perfect mirror as an asymmetric cavity effect, controlled by the quality factor (Q) and the mirror reflection coefficients. Harnessing the photon confinement in the asymmetric cavity explains the basis of the pressure enhancement. We have also discovered that exciting the plasmonic surface wave on the front side or the back side of the Au membrane accompanied with SiN layer will establish a corresponding enhanced pushing and pulling pressure, respectively. This can be easily understood as the surface wave on the front side pushing the membrane and the surface wave on the back side pulling (pushing against the opposite direction to the incident light) the membrane. This provides the physical picture of exciting pushing/pulling pressure from a plane wave illumination. Besides the nanostructure involving metal materials, we have studied and explored the opportunity to excite the pulling and even enhanced pulling pressure on simple all-dielectric material systems (silicon based) with dielectric material in a higher dielectric constant background and by exploiting the nature of evanescent field to the gradient force.

We would like to emphasize conservation of momentum in relation to the enhanced optical pressure presented in Chapter 4. The enhanced net force on the cavity is a result of the cavity asymmetry and quality factor. After establishing the resonance, the momentum exchange between the photons and the cavity satisfy Newton's second law of motion. This can be understood by the analogy of a harmonically oscillating pendulum, where the small external driving force to overcome loss maintains the resonant condition and a large potential/kinetic energy.

REFERENCES

REFERENCES

[1] E. F. Nichols and G. F. Hull, "The pressure due to radiation," *Phys. Rev.*, vol. 17, pp. 26–50, 1903.

[2] P. Lebedev, "Investigations on the pressure forces of light," *Ann. Phys*, vol. 6, pp. 433–458, 1901.

[3] J. C. Maxwell, *A Treatise on Electricity and Magnetism*. Clarendon press, 1881, vol. 2.

[4] A. Ashkin and J. M. Dziedzic, "Radiation pressure on a free liquid surface," *Phys. Rev. Lett.*, vol. 30, no. 4, pp. 139–142, Jan. 1973.

[5] A. Ashkin, J. M. Dziedzic, J. E. Bjorkholm, and S. Chu, "Observation of a single-beam gradient force optical trap for dielectric particles," *Opt. Lett.*, vol. 11, no. 5, pp. 288–290, 1986.

[6] J.-D. Wen, M. Manosas, P. T. Li, S. B. Smith, C. Bustamante, F. Ritort, and I. Tinoco Jr, "Force unfolding kinetics of rna using optical tweezers. i. effects of experimental variables on measured results," *Biophys. J.*, vol. 92, no. 9, pp. 2996–3009, 2007.

[7] J. R. Moffitt, Y. R. Chemla, S. B. Smith, and C. Bustamante, "Recent advances in optical tweezers," *Annu. Rev. Biochem.*, vol. 77, no. 1, pp. 205–228, 2008.

[8] D. J. Wineland and W. M. Itano, "Laser cooling of atoms," *Phys. Rev. A*, vol. 20, no. 4, p. 1521, 1979.

[9] C. Myatt, E. Burt, R. Ghrist, E. A. Cornell, and C. Wieman, "Production of two overlapping bose-einstein condensates by sympathetic cooling," *Phys. Rev. Lett.*, vol. 78, no. 4, p. 586, 1997.

[10] W. D. Phillips, "Nobel lecture: Laser cooling and trapping of neutral atoms," *Rev. Mod. Phys.*, vol. 70, no. 3, p. 721, 1998.

[11] K. J. Webb, "Dependence of the radiation pressure on the background refractive index," *Phys. Rev. Lett.*, vol. 111, p. 043602, July 2013.

[12] M. Mansuripur, "Electromagnetic-force distribution inside matter," *Phys. Rev. A*, vol. 88, p. 023826, 2013.

[13] A. Einstein and J. Laub, "Über die im elektromagnetischen felde auf ruhende körper ausgeübten ponderomotorischen kräfte," *Ann. Phys.*, vol. 331, no. 8, pp. 541–550, 1908.

[14] R. V. Jones and B. Leslie, "The measurement of optical radiation pressure in dispersive media," *Proc. Royal Soc. A*, vol. 360, no. 1702, pp. 347–363, Apr. 1978.

[15] L.-F. Yang, A. Datta, Y.-C. Hsueh, X. Xu, and K. J. Webb, "Demonstration of enhanced optical pressure on a structured surface," *Phys. Rev. Lett.*, vol. 122, p. 083901, 2019.

[16] Y.-C. Hsueh, L.-F. Yang, and K. J. Webb, "Enhanced optical pressure with asymmetric cavities," *Phys. Rev. B*, vol. 99, no. 4, p. 045437, 2019.

[17] Shivanand and K. J. Webb, "Electromagnetic plane wave force on a slab," *J. Opt. Soc. Am. B*, vol. 29, no. 12, pp. 3330–3334, Dec. 2012.

[18] G. K. Campbell, A. E. Leanhardt, J. Mun, M. Boyd, E. W. Streed, W. Ketterle, and D. E. Pritchard, "Photon recoil momentum in dispersive media," *Phys. Rev. Lett.*, vol. 94, p. 170403, 2005.

[19] K. J. Webb and Shivanand, "Negative electromagnetic plane-wave force in gain media," *Phys. Rev. E*, vol. 84, p. 057602, 2011.

[20] ——, "Electromagnetic field energy in dispersive materials," *J. Opt. Soc. Am. B*, vol. 27, no. 6, pp. 1215–1220, June 2010.

[21] ——, "Electromagnetic plane-wave forces on homogeneous material," *J. Opt. Soc. Am. B*, vol. 29, no. 8, pp. 1904–1910, Aug. 2012.

[22] P. Penfield and H. A. Haus, *Electrodynamics of Moving Media*. MIT Press, Cambridge, MA, 1967.

[23] K. J. Webb and Shivanand, "Negative electromagnetic plane-wave force in gain media," *Phys. Rev. E*, vol. 84, no. 5, p. 057602, 2011.

[24] A. H. Velzen and K. J. Webb, "Electromagnetic force on structured metallic surfaces," *Phys. Rev. B*, vol. 92, no. 11, p. 115416, 2015.

[25] "COMSOL Multiphysics," *http://www.comsol.com/products/multiphysics/*.

[26] P. B. Johnson and R. W. Christy, "Optical constants of the noble metals," *Phys. Rev. B*, vol. 6, no. 12, pp. 4370–4379, 1972.

[27] K. J. Webb and J. Li, "Waveguide cavity surface-enhanced raman scattering," *Phys. Rev. B*, vol. 73, no. 7, p. 073404, 2006.

[28] A. Novitsky, C.-W. Qiu, and H. Wang, "Single gradientless light beam drags particles as tractor beams," *Phys. Rev. Lett.*, vol. 107, no. 20, p. 203601, 2011.

[29] J. Canny, "A computational approach to edge detection," in *Readings in Computer Vision*. Elsevier, 1987, pp. 184–203.

[30] J. Rosenberg, Q. Lin, and O. Painter, "Static and dynamic wavelength routing via the gradient optical force," *Nat. Photonics*, vol. 3, no. 8, pp. 478–483, 2009.

[31] D. Nikolova, S. Rumley, D. Calhoun, Q. Li, R. Hendry, P. Samadi, and K. Bergman, "Scaling silicon photonic switch fabrics for data center interconnection networks," *Opt. Express*, vol. 23, no. 2, pp. 1159–1175, 2015.

[32] S. Gigan, H. R. Böhm, M. Paternostro, F. Blaser, G. Langer, J. B. Hertzberg, K. C. Schwab, D. Bäuerle, M. Aspelmeyer, and A. Zeilinger, "Self-cooling of a micromirror by radiation pressure," *Nature*, vol. 444, no. 7115, p. 67, 2006.

[33] A. Schliesser, P. Del'Haye, N. Nooshi, K. J. Vahala, and T. J. Kippenberg, "Radiation pressure cooling of a micromechanical oscillator using dynamical backaction," *Phys. Rev. Lett.*, vol. 97, no. 24, p. 243905, 2006.

[34] A. Dorsel, J. D. McCullen, P. Meystre, E. Vignes, and H. Walther, "Optical bistability and mirror confinement induced by radiation pressure," *Phys. Rev. Lett.*, vol. 51, no. 17, p. 1550, 1983.

[35] T. J. Kippenberg, H. Rokhsari, T. Carmon, A. Scherer, and K. J. Vahala, "Analysis of radiation-pressure induced mechanical oscillation of an optical microcavity," *Phys. Rev. Lett.*, vol. 95, no. 3, p. 033901, 2005.

[36] H. Zhu, F. Yi, and E. Cubukcu, "Plasmonic metamaterial absorber for broadband manipulation of mechanical resonances," *Nat. Photonics*, vol. 10, no. 11, p. 709, 2016.

[37] A. Mizrahi and L. Schächter, "Electromagnetic forces on the dielectric layers of the planar optical bragg acceleration structure," *Phys. Rev. E*, vol. 74, no. 3, p. 036504, 2006.

[38] Shivanand and K. J. Webb, "Electromagnetic plane-wave force on a slab having various constitutive parameters and embedded in a background material," *J. Opt. Soc. Am. B*, vol. 29, no. 12, pp. 3330–3334, 2012.

[39] M. I. Antonoyiannakis and J. B. Pendry, "Electromagnetic forces in photonic crystals," *Phys. Rev. B*, vol. 60, no. 4, p. 2363, 1999.

[40] K. Webb and J. Li, "Analysis of transmission through small apertures in conducting films," *Phys. Rev. B*, vol. 73, no. 3, p. 033401, 2006.

[41] R. E. Collin, *Field Theory of Guided Waves*. McGraw-Hill, 1960.

[42] K. J. Webb and Shivanand, "Electromagnetic field energy in dispersive materials," *J. Opt. Soc. Am. B*, vol. 27, no. 6, pp. 1215–1220, 2010.

[43] M. C. Sanchez, E. Martin, and J. M. Zamarro, "Unified and simplified treatment of techniques for characterising transmission, reflection or absorption resonators," in *Proc. Inst. Elect. Eng., pt. H*, vol. 137, no. 4. IET, 1990, pp. 209–212.

[44] P. J. Petersan and S. M. Anlage, "Measurement of resonant frequency and quality factor of microwave resonators: Comparison of methods," *J. Appl. Phys.*, vol. 84, no. 6, pp. 3392–3402, 1998.

[45] S. Kim, Y. Xuan, V. P. Drachev, L. T. Varghese, L. Fan, M. Qi, and K. J. Webb, "Nanoimprinted plasmonic nanocavity arrays," *Opt. Express*, vol. 21, no. 13, pp. 15 081–15 089, 2013.

[46] Y.-C. Hsueh and K. J. Webb, "Electromagnetic field control with binary aperiodic nanostructures," *J. Opt. Soc. Am. B*, vol. 34, no. 10, pp. 2059–2071, 2017.

[47] J. R. Moffitt, Y. R. Chemla, S. B. Smith, and C. Bustamante, "Recent advances in optical tweezers," *Annu. Rev. Biochem.*, vol. 77, pp. 205–228, 2008.

[48] Y.-C. Hsueh, L.-F. Yang, and K. J. Webb, "Optical pressure control with aperiodic nanostructured material," *J. Opt. Soc. Am. B*, vol. 36, no. 6, pp. 1408–1419, 2019.

[49] K. J. Webb and J. Li, "Resonant slot optical guiding in metallic nanoparticle chains," *Phys. Rev. B*, vol. 72, p. 201402R, 2005.

[50] ——, "Resonant waveguide field enhancement in dimers," *Opt. Lett.*, vol. 31, no. 22, pp. 3348–3350, Nov. 2006.

[51] ——, "Analysis of transmission through small apertures in conducting films," *Phys. Rev. B*, vol. 73, p. 33401, 2006.

[52] J. Li and K. J. Webb, "Terahertz field enhancement in doped semiconductor slot cavities," *J. Appl. Phys.*, vol. 106, p. 124901, 2009.

[53] H. A. Atwater, A. R. Davoyan, O. Ilic, D. Jariwala, M. C. Sherrott, C. M. Went, W. S. Whitney, and J. Wong, "Materials challenges for the starshot lightsail," *Nature materials*, vol. 17, no. 10, p. 861, 2018.

VITA

VITA

Grew up in Taichung City, Taiwan, Li-Fan Yang attended Taichung Municipal First Senior High School. After graduating, Li-Fan went on to National Tsing-Hua University to study Electrical Engineering for Bachelor and Master Degrees from 2005 to 2011. During his Master, Li-Fan worked with Professor Shang-Da Yang on Ultrafast Photonics, characterising ultrashort pulse from nonlinear interference technique and constructing a femto-second pulsed fiber laser. After his M.S., he spent a year in Professor Andy Kung's lab as a research assistant working on octave-spanning coherent supercontinuum wave by Ti-sapphire laser. In Fall 2013, Li-Fan began his Ph.D. program at Purdue University in Professor Kevin J. Webb's group, focusing on optomechanics with optical force and nanophotonics. As a research assistant he contributed to grant proposals and reports, and attended several conferences. The chapters of this dissertation have been submitted for publication in various journals.